

DTIC FILE COPY

(12)

DNA-TR-86-403

AD-A184 509

A COMPARATIVE ANALYSIS OF EQUATORIAL AND AURORAL-ZONE PHASE SCINTILLATION DATA

C. L. Rino
T. M. Dabbs
SRI International
333 Ravenswood Avenue
Menlo Park, CA 94025-3434

1 October 1986



Technical Report

CONTRACT No. DNA 001-86-C-0002

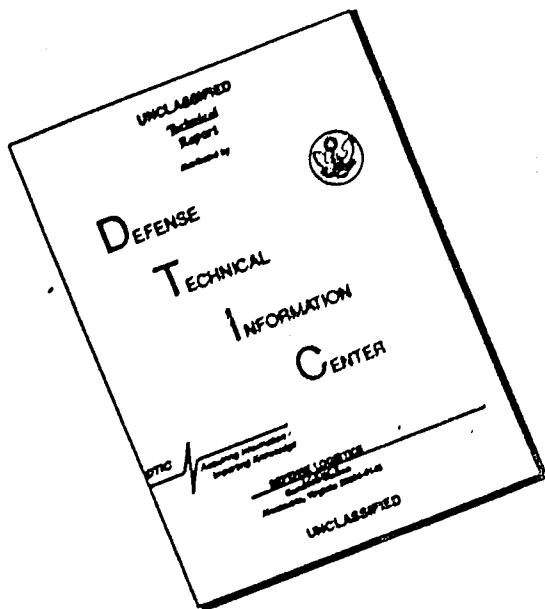
Approved for public release;
distribution is unlimited.

THIS WORK WAS SPONSORED BY THE DEFENSE NUCLEAR AGENCY
UNDER RDT&E RMC CODE B3220867632 RW RA 00001 25904D.

Prepared for
Director
DEFENSE NUCLEAR AGENCY
Washington, DC 20305-1000

87 9 9 292

DISCLAIMER NOTICE



**THIS DOCUMENT IS BEST
QUALITY AVAILABLE. THE COPY
FURNISHED TO DTIC CONTAINED
A SIGNIFICANT NUMBER OF
PAGES WHICH DO NOT
REPRODUCE LEGIBLY.**

Destroy this report when it is no longer needed. Do not return
to sender.

PLEASE NOTIFY THE DEFENSE NUCLEAR AGENCY
ATTN: TITL, WASHINGTON, DC 20305 1000, IF YOUR
ADDRESS IS INCORRECT, IF YOU WISH IT DELETED
FROM THE DISTRIBUTION LIST, OR IF THE ADDRESSEE
IS NO LONGER EMPLOYED BY YOUR ORGANIZATION.



DISTRIBUTION LIST UPDATE

This mailer is provided to enable DNA to maintain current distribution lists for reports. We would appreciate your providing the requested information.

- Add the individual listed to your distribution list.
- Delete the cited organization/individual.
- Change of address.

NAME: _____

ORGANIZATION: _____

OLD ADDRESS

CURRENT ADDRESS

TELEPHONE NUMBER: () _____

SUBJECT AREA(s) OF INTEREST:

DNA OR OTHER GOVERNMENT CONTRACT NUMBER: _____

CERTIFICATION OF NEED-TO-KNOW BY GOVERNMENT SPONSOR (if other than DNA):

SPONSORING ORGANIZATION: _____

CONTRACTING OFFICER OR REPRESENTATIVE: _____

SIGNATURE: _____

CUT HERE AND RETURN



Director
Defense Nuclear Agency
ATTN: █ TITL
Washington, DC 20305-1000

Director
Defense Nuclear Agency
ATTN: █ TITL
Washington, DC 20305-1000

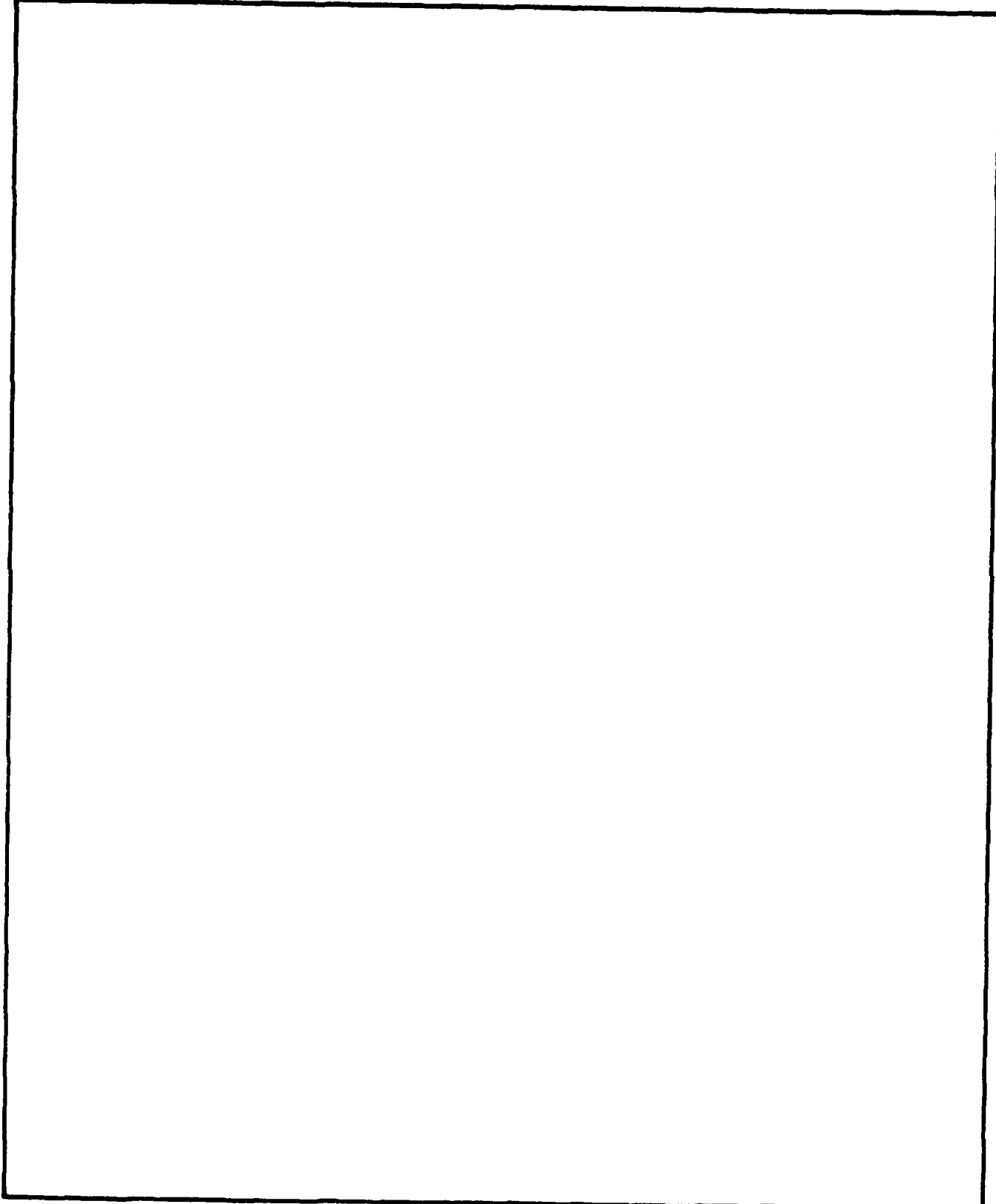
UNCLASSIFIED
SECURITY CLASSIFICATION OF THIS PAGE

ADA184509

REPORT DOCUMENTATION PAGE

1a. REPORT SECURITY CLASSIFICATION UNCLASSIFIED		1b. RESTRICTIVE MARKINGS										
2a. SECURITY CLASSIFICATION AUTHORITY N/A since Unclassified		3. DISTRIBUTION/AVAILABILITY OF REPORT Approved for public release; distribution is unlimited.										
2b. DECLASSIFICATION/DOWNGRADING SCHEDULE N/A since Unclassified		5 MONITORING ORGANIZATION REPORT NUMBER(S) DNA-TR-86-403										
4. PERFORMING ORGANIZATION REPORT NUMBER(S) SRI Project 1700		7a. NAME OF MONITORING ORGANIZATION Director Defense Nuclear Agency										
6a. NAME OF PERFORMING ORGANIZATION SRI International	6b. OFFICE SYMBOL (if applicable)	7b. ADDRESS (City, State, and ZIP Code) Washington, DC 20305-1000										
6c. ADDRESS (City, State, and ZIP Code) 333 Ravenswood Avenue Menlo Park, CA 94025-3434												
8a. NAME OF FUNDING/SPONSORING ORGANIZATION RAAE/Wittwer	8b. OFFICE SYMBOL (if applicable)	9. PROCUREMENT INSTRUMENT IDENTIFICATION NUMBER DNA 001-86-C-0002										
8c. ADDRESS (City, State, and ZIP Code)		10. SOURCE OF FUNDING NUMBERS <table border="1"><tr><td>PROGRAM ELEMENT NO. 62715H</td><td>PROJECT NO. RW</td><td>TASK NO. RA</td><td>WORK UNIT ACCESSION NO. DH200891</td></tr></table>		PROGRAM ELEMENT NO. 62715H	PROJECT NO. RW	TASK NO. RA	WORK UNIT ACCESSION NO. DH200891					
PROGRAM ELEMENT NO. 62715H	PROJECT NO. RW	TASK NO. RA	WORK UNIT ACCESSION NO. DH200891									
11. TITLE (Include Security Classification) A COMPARATIVE ANALYSIS OF EQUATORIAL AND AURORAL-ZONE PHASE SCINTILLATION DATA												
12. PERSONAL AUTHOR(S) Rino, Charles L. and Dabbs, Teri M.												
13a. TYPE OF REPORT Technical	13b. TIME COVERED FROM 850313 TO 860930	14. DATE OF REPORT (Year Month Day) 861001	15. PAGE COUNT 78									
16. SUPPLEMENTARY NOTATION This work was sponsored by the Defense Nuclear Agency under RDT&E RMC Code B3220867632 RW RA 00001 25904D.												
17. COSATI CODES <table border="1"><tr><th>FIELD</th><th>GROUP</th><th>SUB-GROUP</th></tr><tr><td>17</td><td>02</td><td></td></tr><tr><td>20</td><td>09</td><td></td></tr></table>		FIELD	GROUP	SUB-GROUP	17	02		20	09		18. SUBJECT TERMS (Continue on reverse if necessary and identify by block number) Radio-Wave Scintillation Multicomponent Spectra Weak Scatter Spectral Characteristics	
FIELD	GROUP	SUB-GROUP										
17	02											
20	09											
19. ABSTRACT (Continue on reverse if necessary and identify by block number) A comparison is made between equatorial and auroral-zone phase scintillation. The spectral characteristics of weak-scatter phase scintillation data collected at two equatorial ground stations are contrasted with similar data collected at two auroral-zone ground stations. An automated, multisegmented fitting procedure was used to determine these characteristics. Three types of spectra were found. Despite temporal and spatial differences, the two equatorial data sets have similar spectral characteristics. The auroral-zone sets are also similar. In contrast, the spectral characteristics of the two latitude regions are quite different from each other.												
20. DISTRIBUTION AVAILABILITY OF ABSTRACT <input type="checkbox"/> UNCLASSIFIED-UNLIMITED <input checked="" type="checkbox"/> SAME AS RPT <input type="checkbox"/> DTIC USERS		21. ABSTRACT SECURITY CLASSIFICATION UNCLASSIFIED										
22a. NAME OF RESPONSIBLE INDIVIDUAL Sandra E. Young		22b. TELEPHONE (Include Area Code) (202) 325-7042	22c. OFFICE SYMBOL DNA/CSTI									

~~UNCLASSIFIED~~
~~SECURITY CLASSIFICATION OF THIS PAGE~~



~~SECURITY CLASSIFICATION OF THIS PAGE~~

~~UNCLASSIFIED~~

CONVERSION TABLE

Conversion factors for U.S. Customary to metric (SI) units of measurement

MULTIPLY TO GET	BY	TO GET DIVIDE
←	←	←

angstrom	1.000 000 X E -10	meters (m)
atmosphere (normal)	1.013 25 X E +2	kilo pascal (kPa)
bar	1.000 000 X E +2	kilo pascal (kPa)
barn	1.000 000 X E -28	meter² (m²)
British thermal unit (thermochemical)	1.054 350 X E +3	joule (J)
calorie (thermochemical)	4.184 000	joule (J)
cal (thermochemical)/cm²	4.184 000 X E -2	mega joule/m² (MJ/m²)
curie	3.700 000 X E +1	*giga becquerel (GBq)
degree (angle)	1.745 329 X E -2	radian (rad)
degree Fahrenheit	$t_K = (t^{\circ}F + 459.67)/1.8$	degree kelvin (K)
electron volt	1.602 19 X E -19	joule (J)
erg	1.000 000 X E -7	joule (J)
erg/second	1.000 000 X E -7	watt (W)
foot	3.048 000 X E -1	meter (m)
foot-pound-force	1.355 818	joule (J)
gallon (U.S. liquid)	3.785 412 X E -3	meter³ (m³)
inch	2.540 000 X E -2	meter (m)
jerk	1.000 000 X E +9	joule (J)
joule/kilogram (J/kg) (radiation dose absorbed)	1.000 000	Gray (Gy)
kilotons	4.183	terajoules
kip (1000 lbf)	4.448 222 X E +3	newton (N)
kip/inch² (ksi)	6.894 757 X E +3	kilo pascal (kPa)
ktap	1.000 000 X E +2	newton-second/m² (N-s/m²)
micron	1.000 000 X E -6	meter (m)
mil	2.540 000 X E -5	meter (m)
mile (international)	1.609 344 X E +3	meter (m)
ounce	2.834 952 X E -2	kilogram (kg)
pound-force (lbs avoirdupois)	4.448 222	newton (N)
pound-force inch	1.129 848 X E -1	newton-meter (N·m)
pound-force/inch	1.751 268 X E +2	newton/meter (N/m)
pound-force/foot²	4.788 026 X E -2	kilo pascal (kPa)
pound-force/inch² (psi)	6.894 757	kilo pascal (kPa)
pound-mass (lbm avoirdupois)	4.535 924 X E -1	kilogram (kg)
pound-mass-foot² (moment of inertia)	4.214 011 X E -2	kilogram-meter² (kg·m²)
pound-mass/foot³	1.601 846 X E +1	kilogram/meter³ (kg/m³)
rad (radiation dose absorbed)	1.000 000 X E -2	*Gray (Gy)
roentgen	2.579 760 X E -4	coulomb/kilogram (C/kg)
shake	1.000 000 X E -8	second (s)
slug	1.459 390 X E +1	kilogram (kg)
torr (mm Hg, 0° C)	1.333 22 X E -1	kilo pascal (kPa)

*The becquerel (Bq) is the SI unit of radioactivity; 1 Bq = 1 event/s.

**The Gray (Gy) is the SI unit of absorbed radiation.

TABLE OF CONTENTS

Section	Page
CONVERSION TABLE	iii
LIST OF ILLUSTRATIONS	v
LIST OF TABLES	vii
1 INTRODUCTION	1
2 DATA ANALYSIS	6
2.1 General Approach	6
2.2 Equatorial Data	7
2.3 Auroral-Zone Data	26
3 DISCUSSION	43
4 LIST OF REFERENCES	48
Appendix	
An Algorithm for Segmented Linear-Curve Fits	53

Accession For	
NTIS CRA&I	<input checked="" type="checkbox"/>
DTIC TAB	<input type="checkbox"/>
Unannounced	<input type="checkbox"/>
Justification	
By _____	
Distribution/	
Availability Codes	
Dist	Avail and/or Special
A-1	



LIST OF ILLUSTRATIONS

Figure		Page
1	Distributions of equatorial intensity and phase scintillation	10
2	Frequency comparisons of intensity and phase scintillation	11
3	Distribution of v_{eff}	13
4(a)	Occurrence of spectral types and power-law indices for Type 1 spectra--Kwajalein	14
4(b)	Occurrence of spectral types and power-law indices for Type 1 spectra--Ancon	15
5(a)	Spectral index and break frequency distribution for Type 2 spectra--Kwajalein	16
5(b)	Spectral index and break frequency distribution for Type 2 spectra--Ancon	17
6(a)	Spectral index and break frequency distribution for Type 3 spectra--Kwajalein	18
6(b)	Spectral index and break frequency distribution for Type 3 spectra--Ancon	19
7	Type 1 spectral index plotted against L-band S_4	23
8	Type 2 p_A spectral index plotted against L-band S_4	25
9	Variation of S_4 and p with C_s as inferred from low-resolution in situ data and corresponding S_4 variation	27
10	Distributions of auroral zone intensity and phase scintillation	30
11	Frequency comparisons of intensity and phase scintillation	31

LIST OF ILLUSTRATIONS (CONCLUDED)

Figure	Page
12(a) Distribution of v_{eff} --Poker Flat	32
12(b) Distribution of v_{eff} --Tromso	33
13(a) Occurrence of spectral types and power-law indices for auroral zone Type 1 spectra--Poker Flat	34
13(b) Occurrence of spectral types and power-law indices for auroral zone Type 1 spectra--Tromso	35
14(a) Spectral index and break frequency distributions for auroral-zone Type 3 spectra--Poker Flat	37
14(b) Spectral index and break frequency distributions for auroral-zone Type 3 spectra--Tromso	38
15(a) Invariant latitude dependence of auroral zone spectral indices--Poker Flat, S_4 : 0.2 to 0.5	41
15(b) Invariant latitude dependence of auroral zone spectral indices--Tromso, S_4 : 0.2 to 0.5	42
16 Linear fit versus multisegment fit	56
17 Overall trend determined from least-squares polynomial fit	59
18 Tangents to polynomial that are parallel to overall trend	61
19 Linear least-squares fits to data over each estimated linear region	62
20 Linear least-squares fits to polynomial over each estimated linear region	63
21 Multisegment fit to data	64
22 Multisegment fit to polynomial representation of the data	65

LIST OF TABLES

Table	Page
1 Summary of Equatorial Passes	9
2 Summary of Spectral Characteristics	22
3 Summary of Auroral-Zone Passes	28
4 Summary of Auroral-Zone Spectral Characteristics	39

SECTION 1

INTRODUCTION

Radio-wave scintillation has been used extensively to study irregularities in a variety of transmission media; moreover, with continued improvements in technology and data analysis procedures, additional details of the irregularity characteristics are coming into focus. Yeh and Liu [1982]* reviewed the interpretation of ionospheric scintillation data, which is our interest here. The essential features of the theory can be illustrated by considering the simplest model--a thin scattering layer. Under weak scattering conditions, the average spectrum of the intensity scintillation measured in a plane perpendicular to the propagation direction admits the representation

$$\Phi_I(K) = 4r_e^2 \lambda^2 \Delta L \Phi_{N_e}(K, 0) \sin^2(K^2 l_f^2) , \quad (1)$$

where r_e is the classical electron radius, λ is the wavelength, ΔL is the layer thickness, and $\Phi_{N_e}(K, K_z)$ is the three-dimensional spectrum of the electron-density structure evaluated with $K_z = 0$ where K_z lies along the propagation direction, z . The Fresnel radius, l_f , is defined as

$$l_f = \sqrt{\lambda z / (4\pi)} . \quad (2)$$

* References are listed in alphabetical order in Section 4.

The term $\sin^2(K^2 t_f^2)$ in Eq. (1) substantially alters the otherwise direct mapping of the in situ structure as characterized by $\Phi_{N_e}(K, K_z)$, particularly for spatial frequencies smaller than $2\pi/t_f$. If the structure is uniformly distributed along an extended path but still produces only weak scattering, there is an additional filter function that acts to limit the depth of the K -dependent oscillations. Thus, the pronounced diffraction nulls predicted by Eq. (1) are rarely observed in actual data [Crane, 1976], but the high-pass filter characteristic is preserved.

For phase scintillation, the representation corresponding to Eq. (1) is

$$\Phi_\phi(K) = r_e^2 \lambda^2 \Delta L \Phi_{N_e}(K, 0) \cos^2(K^2 t_f^2) , \quad (3)$$

which is similar, but there is no attenuation for $K < 1/t_f$. Thus, the envelope of $\Phi_\phi(K)$ is, potentially, a more direct mapping of the in situ irregularity structure than the corresponding envelope of $\Phi_I(K)$. Nonetheless, the intensity spectrum generally provides the most consistent measure of scintillation strength through the scintillation index S_4 , defined by the relation

$$S_4^2 = \langle I^2 \rangle / \langle I \rangle^2 - 1 = \iint_{-\infty}^{\infty} \Phi_I(K) dK / (2\pi)^2 . \quad (4)$$

The intrinsic suppression of $\Phi_{N_e}(K, 0)$ in $\Phi_I(K)$ for $K \ll t_f^{-1}$ separates trend-like variations from the more homogeneous random structure. Thus, as long as S_4 is less than unity, it can be used as a measure of the overall perturbation level [Rino and Liu, 1982].

We can only measure a time series generated by the combined motion of the source and the irregularities. The envelope of $\Phi_\phi(K)$ cannot be obtained directly; however, if the irregularities do not change over the time of the measurement, a time-to-space translation can be specified in

terms of an effective scan velocity, v_{eff} . For example, the phase temporal-frequency power spectrum, $\phi_\phi(f)$, is related to $\phi_\phi(K)$ by the integral

$$\phi_\phi(f) = \int_{-\infty}^{\infty} \phi_\phi[(K_y v_y - 2\pi f)/v_x, K_y] dK_y / (2\pi) , \quad (5)$$

where $v_{\text{eff}} = (v_x, v_y)$. Yeh and Liu [1982] discuss the additional smearing that can occur when the structure undergoes internal rearrangement while the measurement is being made.

From this discussion, it follows that to interpret measured scintillation power spectra, the combined effects of changing geometry and diffraction, as well as the weak-scatter limitation, must be assessed. By considering a uniform power-law spectral-density function of the form

$$\phi_{N_e}(K, K_z) \approx C_s q^{-(n+2)} , \quad (6)$$

where q is the magnitude of a quadratic form in K_x , K_y , and K_z (as described in Rino [1982]), some simple limiting forms result. For example, when $f > v_{\text{eff}}/(2\pi l_f)$, the intensity power spectrum is

$$\phi_I(f) \approx 4T f^{-P} , \quad (7)$$

where

$$P = n + 1 . \quad (8)$$

The definition of T depends on n [Rino, 1982], but Eq. (8) shows that the power-law index of the intensity power spectrum beyond the Fresnel cutoff is simply related to the one-dimensional spectral index, n . Similarly, the phase power spectrum in a single power-law environment satisfies the relation

$$\phi_{\phi}(f) \approx T f^{-p} , \quad (9)$$

essentially over the entire range of f ; moreover, the fundamental features of these results are preserved in an extended medium--although the relation between T and C_s becomes more complicated.

In previous analyses of scintillation data from the Wideband satellite [Fremouw et al., 1978; Rino, 1979; Fremouw, 1980; Livingston et al., 1981; Secan and Fremouw, 1983; Fremouw and Robins, 1985], the model outlined above was used. A large body of data was summarized by performing log-linear least-squares fits to the measured phase spectra over fixed temporal frequency ranges. As described in Livingston et al. [1981] and Rino [1979], both the equatorial and auroral-zone data showed fairly shallow and, in the case of the equatorial data, systematically varying spectral indices. The main characteristics of the equatorial irregularities have been confirmed by in situ measurements, which also revealed a more complicated two-component form for the in situ irregularity structure [Livingston et al., 1981; Rino et al., 1981a; Basu and Basu, 1983; LaBelle and Kelley, 1986]. More recent analyses of other scintillation data have also shown evidence of two-component spectra [Franke and Liu, 1983; Bhattacharyya and Rastogi, 1985]. Comparable analyses of auroral-zone data have just begun, but it appears that similar results apply [Villain et al., 1986].

In light of these new results, it was appropriate to reanalyze at least a representative subset of the equatorial and auroral-zone data from the Wideband satellite experiment. We looked for evidence of multicomponent spectra and compared the data with those that are currently being acquired with the HILAT satellite (which was launched into an 82 degree inclination circular orbit at 830-km altitude in June 1983). VHF and UHF amplitude and phase scintillation data from the HILAT satellite have been collected at ground stations in Sondre Stromfjord (Greenland), Tromso (Norway), Fort Churchill (Canada), and Bellevue (Washington), but we shall consider only the data from the auroral-zone station at Tromso in this comparative study.

Ideally, to perform such an analysis, we would use numerical computations with an hypothesized spectral form in the weak-scatter theory and would compare the predictions to the measured spectra. This requires extensive computation, however, and it is practical only for small amounts of data. Where multifrequency data are available, as with Wideband and HILAT, the measured power spectra can be tested for adherence to the frequency dependence predicted by the weak-scatter theory. For example, Eq. (8) is frequency independent, and Eqs. (7) and (9) scale inversely with frequency squared. The Fresnel nulls themselves, which depend on wavelength and distance through Eq. (2), can also be measured. In a companion report [Livingston and Dabbs, 1986 (hereafter referred to as Report I)], this procedure was used both to establish the limits of the weak-scatter theory and to determine the contaminating effects of the diffraction nulls in measuring the characteristics of multicomponent spectra. It was found that the most accurate results are obtained by fitting individual power-law segments adjacent to the first diffraction null.

It is desirable, however, to have an automated procedure that can be routinely applied to the very large data bases that have already been and, in the case of HILAT, continue to be accumulated. To this end, a curve-fitting procedure has been developed that will search for a specified maximum number of power-law segments. Both the power-law segments and the break frequencies are determined automatically and consistently. Because the curve-fitting procedure has a variety of applications, it is described in detail in the Appendix. In the remainder of this report, we describe (1) the results of applying the automated curve-fitting procedure to the old Wideband equatorial and auroral-zone data, and, (2) in the latter case, the comparisons to more recently acquired HILAT auroral-zone scintillation data. The independent analysis of the equatorial data summarized in Report I provides a basis for identifying any contamination caused by departures from strict power-law behavior, which is induced by the diffraction nulls.

SECTION 2

DATA ANALYSIS

2.1 GENERAL APPROACH.

From the discussion in the Introduction, it is clear that even in the case of weak scattering, it is difficult to fully accommodate all of the effects that can influence the interpretation of the scintillation spectra in terms of the structure of the in situ irregularities. On the other hand, certain characteristics of the measured spectra seem to have a robust relation to the corresponding in situ characteristic. For example, the power-law-index relation given by Eq. (8) does not depend on the geometry or θ_f . Of course, if the local value of the spectral index (or any other characteristics of the in situ structure) varies along the propagation path, we will infer a weighted average value, but this problem is inherent in any integral measure, and it must ultimately be resolved by detailed modeling and by comparisons with in situ measurements, which are being pursued separately.

In our analysis here, we accept the fundamental limitation of the integral measure and look for evidence of multicomponent power-law structures. Intuitively, we expect that as long as each power-law segment subtends a large enough range of scale sizes, relations such as Eqs. (7) and (9) can be applied to each power-law segment. This is discussed in Rino and Owen [1982], and has been demonstrated in numerical simulations [Franke and Liu, 1983; Rino and Owen, 1984]. Analytic relations between parameters that characterize the three-dimensional, multicomponent in situ spectra and the measurable spectral-strength parameters are more illusive, but good approximations are beginning to emerge [Wittwer, 1986].

In our data analysis, we use the intensity scintillation level to ensure that we are within the confines of the weak-scatter theory as summarized in Section 1, and we look for evidence of multicomponent spectra in the phase scintillation data. Using the Wideband satellite data, phase scintillation was measured simultaneously at VHF (138 MHz), UHF (413 MHz), and L band (1239 MHz). At UHF, seven closely-spaced frequencies were available. These data have been used to establish the maximum scintillation level for which the weak-scatter theory applies, as described in Report I. The data are processed in overlapping 30-s segments; both linear detrending and windowing are applied prior to standard spectral analysis using digital Fourier transforms. The spectral estimates are then interpolated onto a uniform logarithmic grid, and the curve-fitting procedure described in the Appendix is applied. Thus, our summary data consist of a number of power-law segments that are characterized individually by a strength measure, a power-law index, and a break frequency.

The limitations of the curve-fitting procedure itself are discussed in the Appendix. Ultimately, however, we rely on the internal consistency of the results against our understanding of the propagation theory and their relation to other results to verify the numerous manipulations performed in the course of analyzing the data. Our principal concerns in this regard are the potential biases induced by diffraction effects and the departures from the weak-scatter theory--both of which are discussed in Report I. We shall refer to any functional dependence on f_f as a diffraction effect.

2.2 EQUATORIAL DATA.

The general morphology of scintillation occurrence as deduced from Wideband satellite data has been summarized by Livingston [1980]. For our analysis here, 19 passes from the Kwajalein station and 24 passes from the Ancon, Peru, station were selected. This same data set was used in previous studies [Rino and Owen, 1981, 1982; Rino et al., 1981b]. The individual passes were drawn from active nighttime periods

but encompass a wide range of activity levels and elevation angles. The passes are identified in Table 1. Figure 1 summarizes the distributions of intensity and phase scintillation. The ordinates measure the percent occurrence of the abscissae, which are identified on the individual histograms. In Figure 2 we show scatter plots of the measured UHF and VHF S_4 indices plotted against the logarithm of the L-band S_4 index (top row of plots) together with scatter plots of the measured rms phase at adjacent frequencies (bottom row of plots).

Several points should be noted. From Figure 1, we see that the scintillation levels reach saturation ($S_4 \sim 1.0$) at VHF, moderate values at UHF, but are generally weak at L band. Thus, most of the VHF data cannot be analyzed using the weak-scatter theory. The saturation of the VHF S_4 values is more clearly displayed in Figure 2; moreover, a careful inspection of the data shows that a small subset of the VHF S_4 values exceed unity. This so-called strong-focusing effect in power-law environments is indicative of an outer-scale cutoff or contributions from steeply-sloped power laws [Rino and Owen, 1984; Jakeman, 1982]. Evidently, it was not observed in our earlier analyses because of the shorter data intervals (10 s versus 30 s) [Rino and Liu, 1982]. Turning to the phase data, a necessary condition for negligible diffraction effects, as we defined them above, is a linear dependence of the rms phase on frequency. The L-band and UHF data follow the linear relation to nearly 5 rad of rms phase, but the corresponding VHF-UHF data in Figure 2 show significant departures, which are indicative of strong-scatter effects that are not accommodated in the theory outlined in Section 1.

In our summary analysis of the phase spectra, we consider only data segments for which the S_4 value at the particular frequency lies between 0.2 and 0.5. The lower limit is used to avoid noise contamination in

Table 1. Summary of equatorial passes.

File	Day	Start (U)	End (UT)	Number of Records
KWAJALEIN 1977 (Midnight = 12:00 UT)				
1	188	12:13:32	12:25:02	47
2	189	12:53:34	13:04:04	43
3	209	12:13:28	12:23:58	43
4	212	12:27:12	12:38:42	47
5	216	13:23:12	13:31:17	44
6	218	12:57:12	13:07:42	43
7	224	11:42:32	11:53:17	44
8	226	11:18:42	11:27:12	35
9	226	13:01:52	13:12:07	42
10	228	12:36:22	12:47:52	46
11	229	11:32:42	11:42:42	41
12	229	13:17:02	13:26:17	37
13	232	11:46:52	11:58:07	46
14	234	11:22:52	11:32:07	38
15	235	12:01:22	12:12:52	47
16	237	13:21:52	13:30:22	35
17	238	12:15:52	12:27:07	46
18	241	12:30:52	12:42:22	47
19	250	11:31:29	11:41:59	43
ANCON 1977 (Midnight = 4:00 UT)				
1	40	4:40:52	4:52:22	47
2	42	4:15:52	4:27:22	47
3	49	3:41:32	3:53:02	47
4	63	4:15:12	4:26:42	47
5	74	4:35:22	4:46:52	47
6	75	3:31:52	3:41:52	41
7	76	4:10:22	4:21:52	47
8	78	3:46:02	3:57:02	45
9	79	4:25:12	4:36:42	47
10	80	3:22:12	3:31:12	37
11	80	5:05:32	5:15:47	42
12	81	4:00:32	4:12:02	47
13	82	4:40:02	4:51:32	47
14	83	3:36:22	3:46:37	42
15	83	5:21:02	5:30:02	37
16	85	4:55:12	5:06:12	45
17	88	3:26:42	3:36:12	39
18	88	5:10:22	5:20:22	41
19	89	4:05:02	4:16:32	47
20	90	4:44:42	4:56:12	47
21	96	3:31:02	3:41:17	42
22	103	4:39:12	4:50:42	47
23	104	3:35:32	3:46:17	44
24	110	4:04:22	4:15:52	47

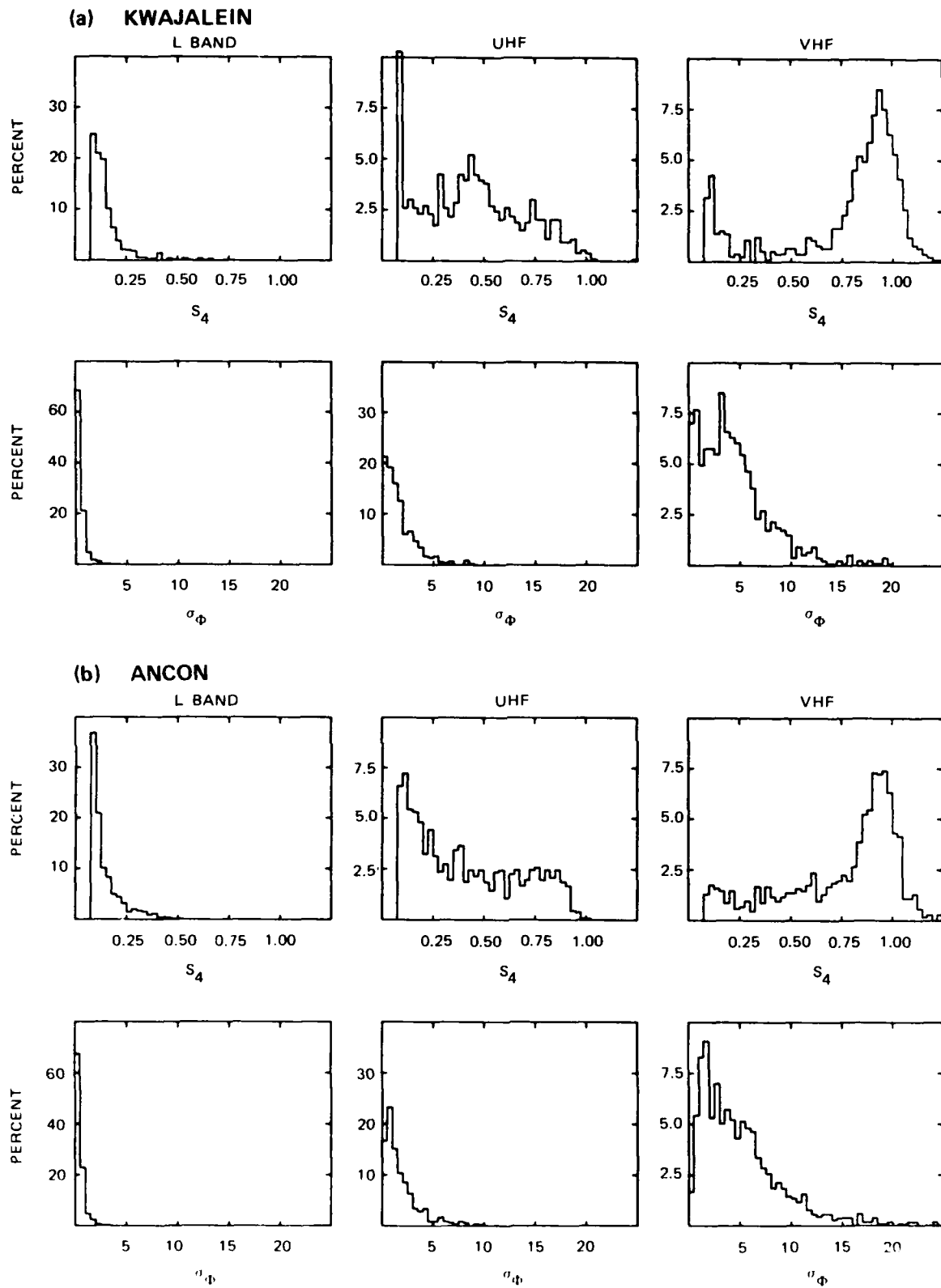


Figure 1. Distributions of equatorial intensity and phase scintillation.

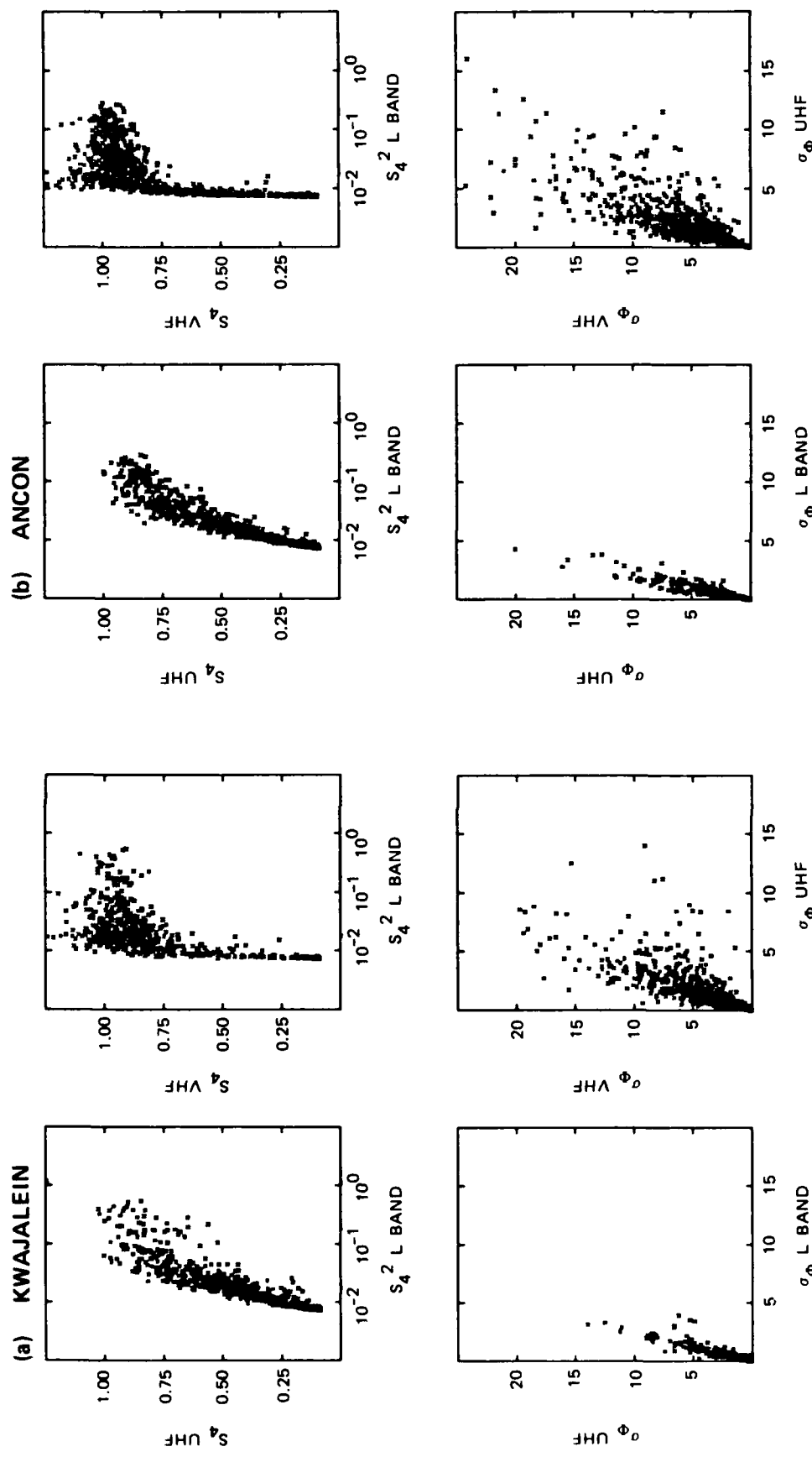


Figure 2. Frequency comparisons of intensity and phase scintillation.

the midrange of the temporal frequencies that contribute to the power spectra. The upper limit was established by performing a detailed analysis of the closely-spaced UHF scintillation data, as discussed in Report I.

The scintillation at each frequency is characterized separately. To convert the temporal frequencies to spatial frequencies, we use the effective scan velocity as defined in Rino [1982] for an axial ratio of 100:1. The basic assumption here is that the anisotropy of the in situ spectrum can be characterized by a quadratic form--irrespective of the overall spectral shape. For equatorial data, the strict validity of this assumption is not too critical. Indeed, near the geomagnetic equator, v_{eff} is nearly equal to the component of the relative penetration-point velocity perpendicular to the propagation path for axial ratios greater than 10:1. In Figure 3, we have plotted the distributions of v_{eff} for the equatorial passes. The relatively small values of v_{eff} compared with the actual penetration-point velocity of ~ 3 km/s result from the highly inclined, sun-synchronous orbit of the Wideband satellite, which places the descending passes nearly along the geomagnetic meridian.

To characterize the weak-scatter phase spectra in terms of the power-law segments found by applying the curve-fitting procedure described in the Appendix, we use the occurrence of breaks in the middle-frequency range ($0.32 \text{ Hz} < f < 3.2 \text{ Hz}$). Short power-law segments that lie outside this range are ignored. Using this procedure, all of the measured spectra were found to be one of three types: (1) single-component power laws, (2) two-component power laws with $p_A < p_B$, and (3) two-component power laws with $p_A > p_B$. In Figures 4, 5, and 6, we summarize the spectral characteristics of the subset of the phase scintillation data segments at each frequency, that satisfy the weak-scatter criteria $0.2 < S_4 < 0.5$.

The first columns in Figure 4 contain histograms of the S_4 values that satisfy the weak-scatter limits. The VHF data have the smallest populations because most of the data are too strongly disturbed;

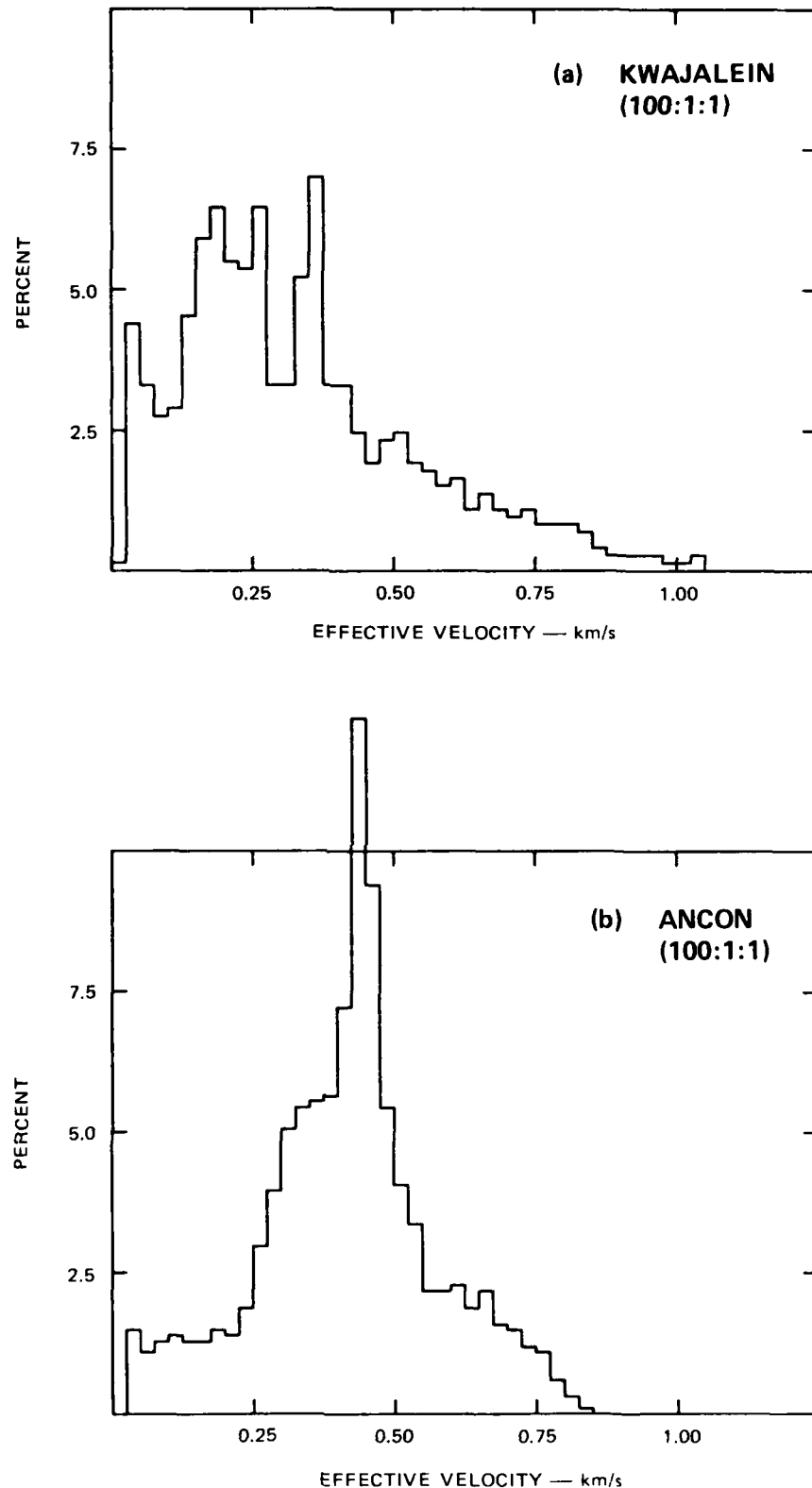
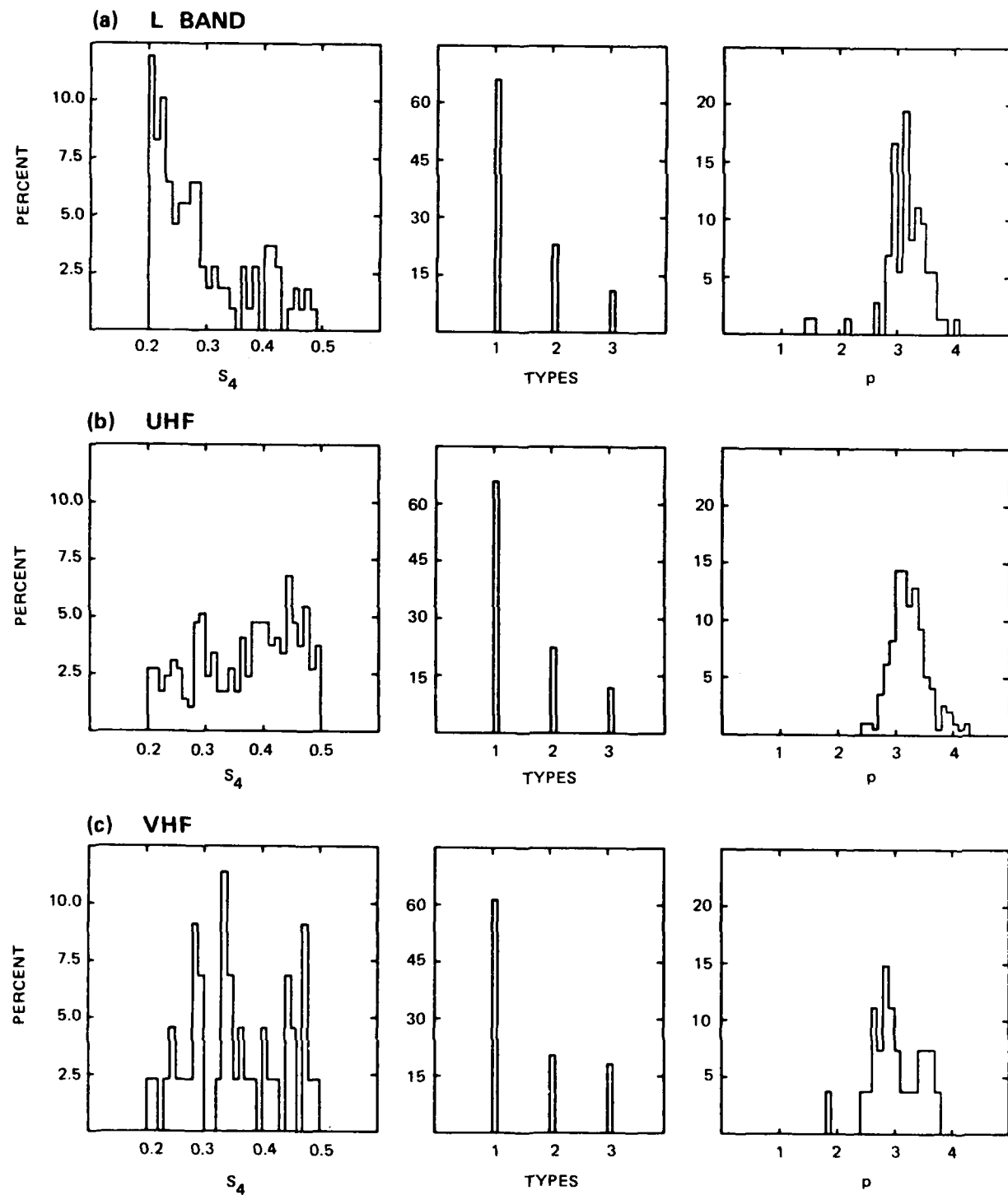


Figure 3. Distribution of v_{eff} .



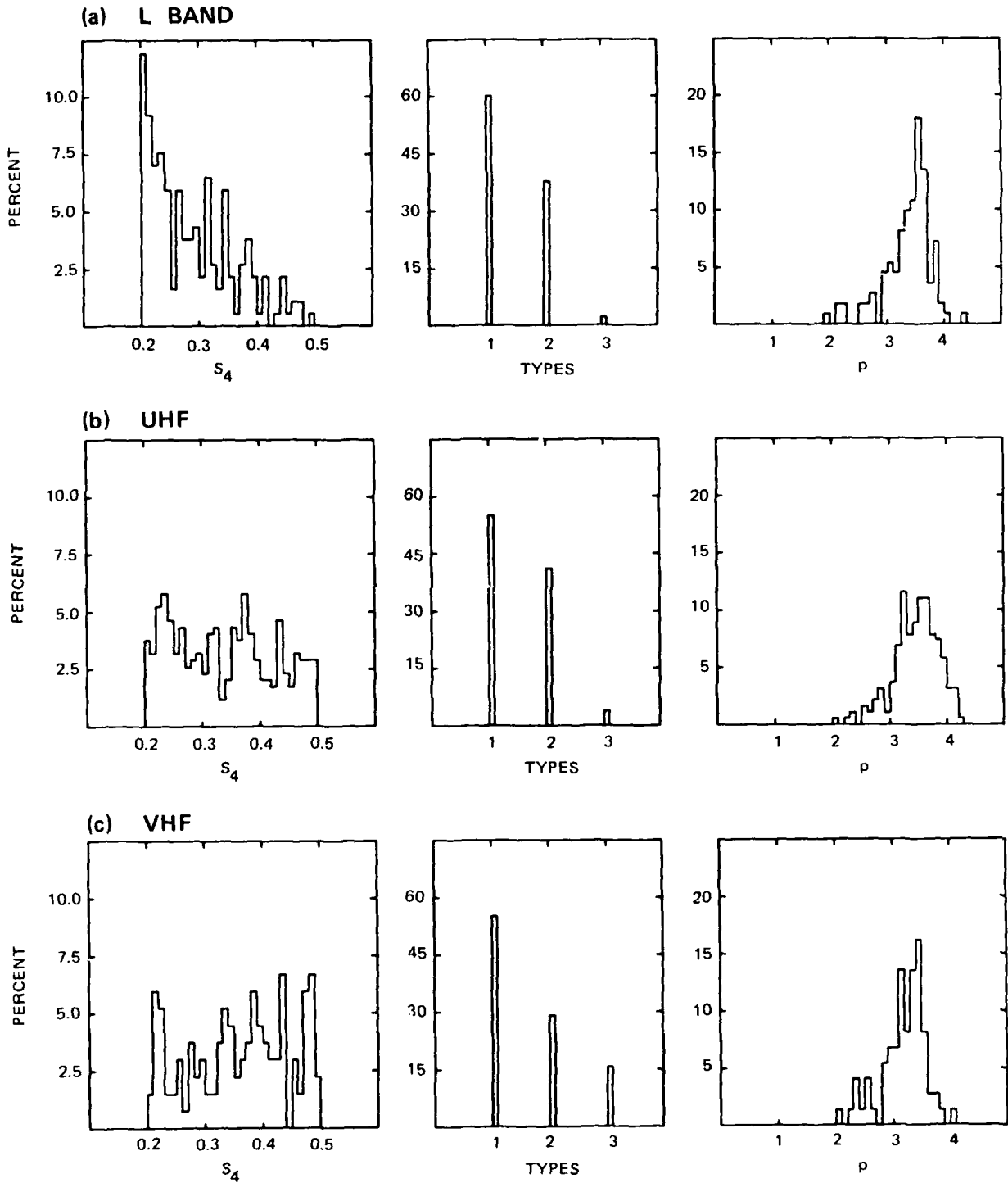


Figure 4(b). Occurrence of spectral types and power-law indices for Type 1 spectra--Ancon.

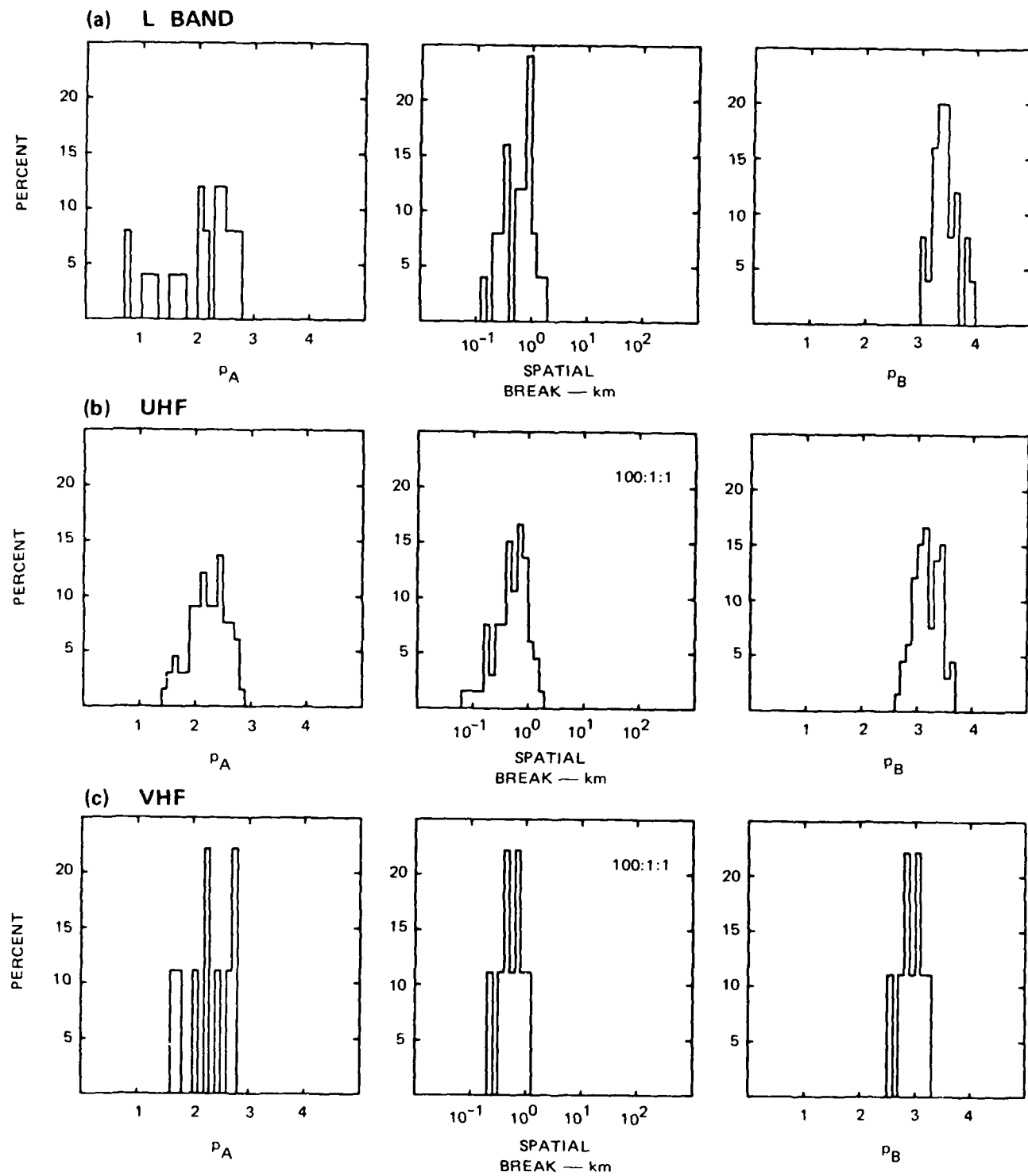


Figure 5(a). Spectral index and break frequency distribution for Type 2 spectra-- Kwajalein.

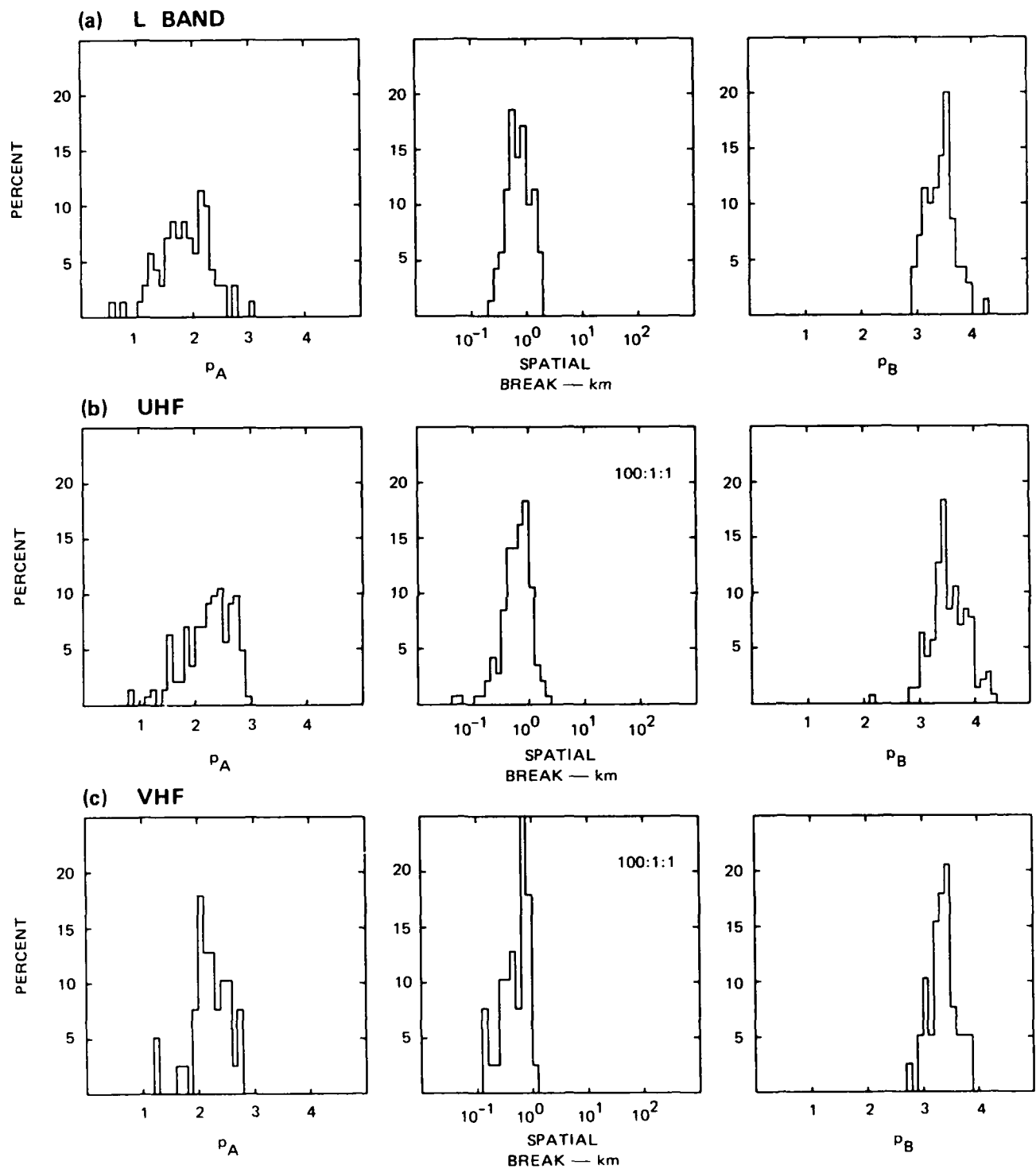


Figure 5(b). Spectral index and break frequency distribution for Type 2 spectra -- Ancon.

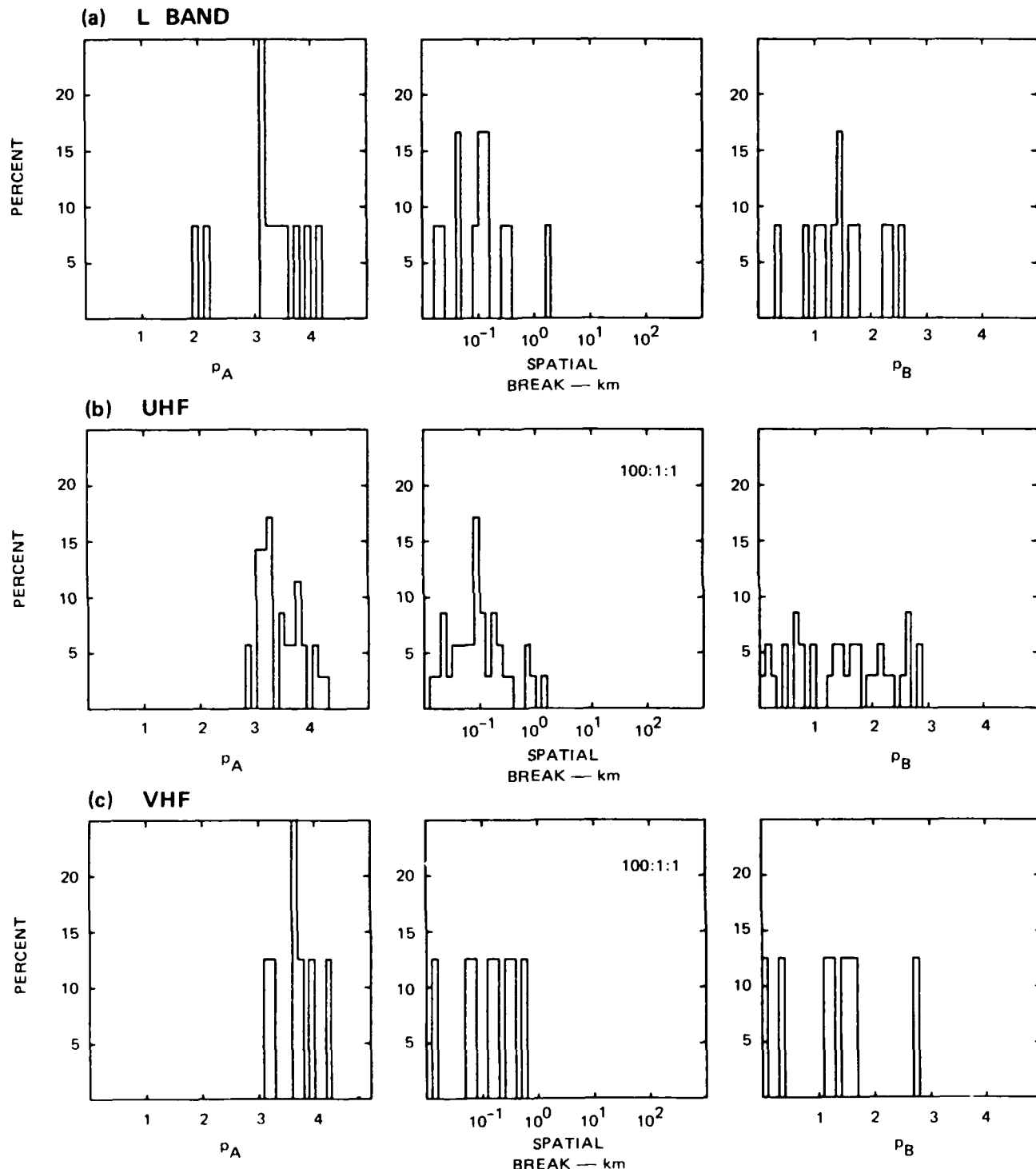


Figure 6(a). Spectral index and break frequency distribution for Type 3 spectra -- Kwajalein.

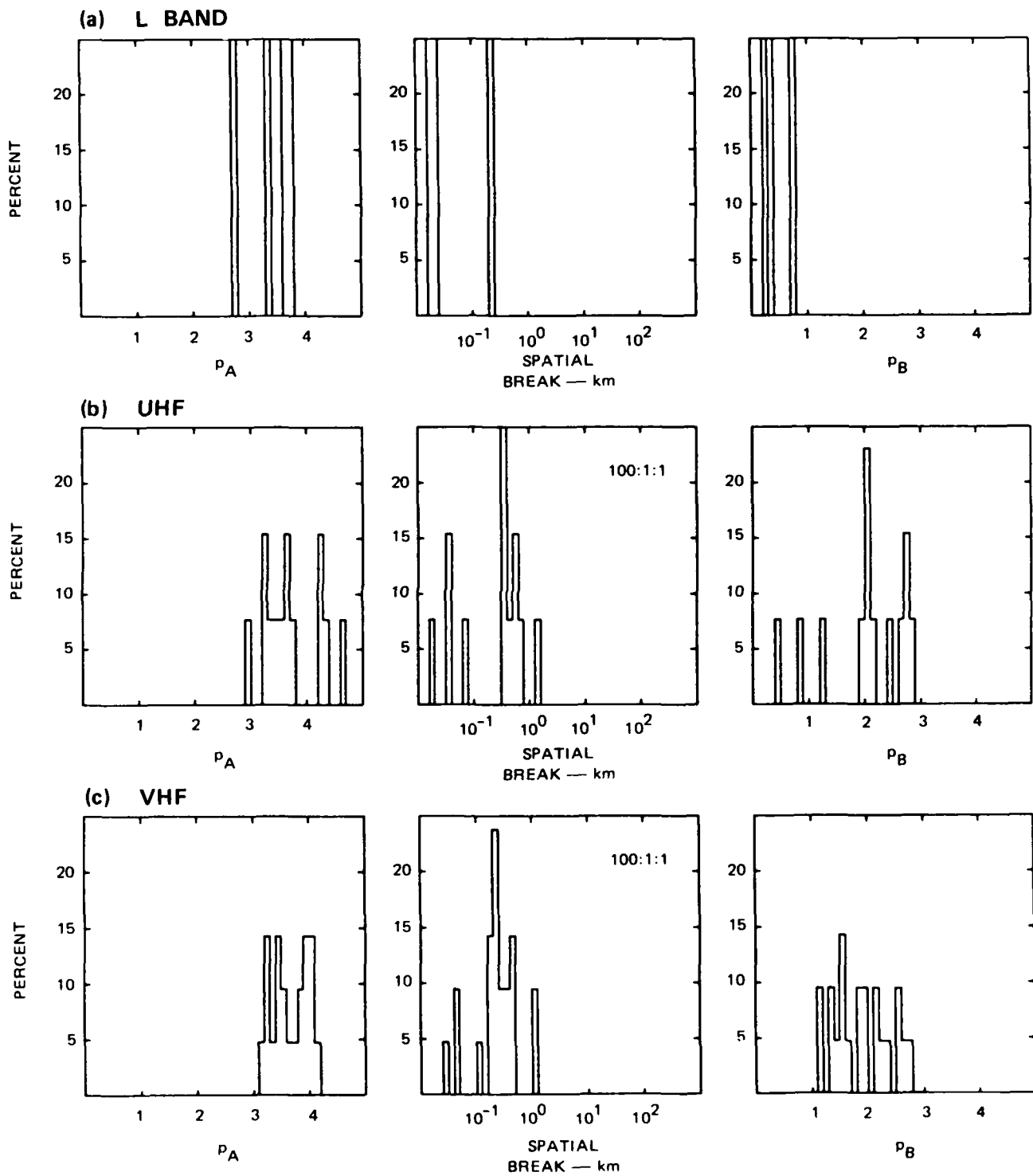


Figure 6(b). Spectral index and break frequency distribution for Type 3 spectra -- Ancon.

moreover, the L-band data are typically near the lower limit. The center columns contain the distributions of the spectral types as described above, and the right-hand columns contain the distributions of the spectral index values for the single power-law spectra that we have referred to as Type 1.

Using this sorting criteria, we find that more than half of the data segments admit a single power-law characterization. The average power-law index value is near but somewhat greater than 3. The Kwajalein data give slightly shallower p indices than the Ancon data, but the Kwajalein data have a higher noise floor because a smaller antenna was used. Thus, we suspect that noise is biasing the Kwajalein data, particularly at VHF, and the differences are probably not significant. The fact that the single power-law segments are not confined to the weaker absolute perturbations is, however, significant. Indeed, the fraction of the samples that admits a single-component characterization is essentially the same at each frequency. In the in situ rocket data summarized in Section 1, single-component power-law spectra were observed primarily in regions of low electron density, such as within depletions or at higher altitudes. Unless such structures are distributed along a highly extended propagation path, we would not expect them to be associated with the strongest scintillation.

The characteristics of the two-component Type 2 spectra are summarized in Figure 5. The first columns show the distributions of p_A . The center columns show the distributions of break frequencies converted to length units using v_{eff} . The right-hand columns show the distributions of p_B . The corresponding data for the Type 3 spectra, which are included primarily for completeness, are shown in Figure 6. Indeed, the number of samples of Type 3 spectra is sufficiently small that we suspect their occurrence to be spurious. Thus, we shall only summarize the detailed structure of the Type 2 spectra.

We first note that p_A is generally less than 3, while p_B is greater than 3; moreover, the distributions of p_B show less spread than the p_A distributions. As with the p distributions, the p_B distributions from

the Kwajalein data are slightly shallower than the corresponding distributions from the Ancon data. We attributed this to noise contamination, and it follows that the higher sensitivity Ancon data are most accurately reflecting the high-frequency and single power-law spectral-index values; however, the details of the data selection and the curve-fitting procedures have subtle effects on the results. The sorting criteria used here combined with the tendency of the curve fitter to respond to abrupt changes outside the middle-frequency range evidently maximize the number of Type 1 spectra. The procedure used in Report I, for example, produced somewhat larger percentages of Type 2 spectra.

The distributions of the break points shown in Figure 5 encompass the values reported from in situ rocket [Rino et al., 1981a; LaBelle and Kappay, 1986] and satellite [Basu and Basu, 1983] measurements; however, there is a systematic increase in the break scale in going from UHF to L band. If this were truly reflecting a structure change, it would be indicative of a perturbation strength dependence of the break frequency, as discussed below. Report I, however, shows that the first Fresnel null in the phase scintillation data falls very near the break frequency, and is undoubtedly biasing the measurement. Thus, we believe that the variation of the break frequency is a bias such that the L-band value is closest to the in situ value. The measured spectral characteristics are summarized in Table 2 together with the number of samples for each spectral type.

Because we have based our data selection on the S_4 levels at each frequency, we have effectively sorted the data by perturbation strength. The L-band data that exceed the lower S_4 limit arise from the largest path-integrated in situ perturbation levels; the UHF data are next. The VHF data that fall below the upper S_4 limit correspond to the smallest path-integrated in situ perturbation levels. The single-component spectra has almost no variation with the frequency at which the spectra are measured. This can be seen more clearly in Figure 7 where we have plotted the measured VHF and L-band p indices against the corresponding

Table 2. Summary of spectral characteristics derived using multicomponent curve-fitting procedure.

Frequency	Type	No. of Data Samples/Total	Spectral Index (p or P_A, P_B)	Break (m)
KWAJALEIN				
VHF	1	27/44	3.02	---
UHF	1	194/295	3.24	---
L Band	1	72/109	3.16	---
VHF	2	9/44	2.29, 2.96	540
UHF	2	66/295	2.23, 3.18	490
L Band	2	25/109	2.04, 3.43	580
VHF	3	8/44	---	---
UHF	3	35/295	---	---
L Band	3	12/109	---	---
ANCON				
VHF	1	74/134	3.18	---
UHF	1	190/345	3.46	---
L Band	1	111/185	3.36	---
VHF	2	39/134	2.21, 3.35	480
UHF	2	142/345	2.24, 3.54	590
L Band	2	70/185	1.86, 3.43	720
VHF	3	21/134	---	---
UHF	3	13/345	---	---
L Band	3	4/185	---	---

*These results are subject to small biases caused by the residual diffraction null that falls near the break frequency. Based on the analysis in Report I, we believe that the most representative median values for the Type 2 spectra are $p_A = 2.3$, $p_B = 3.9$, and $\lambda_B = 650$ m.

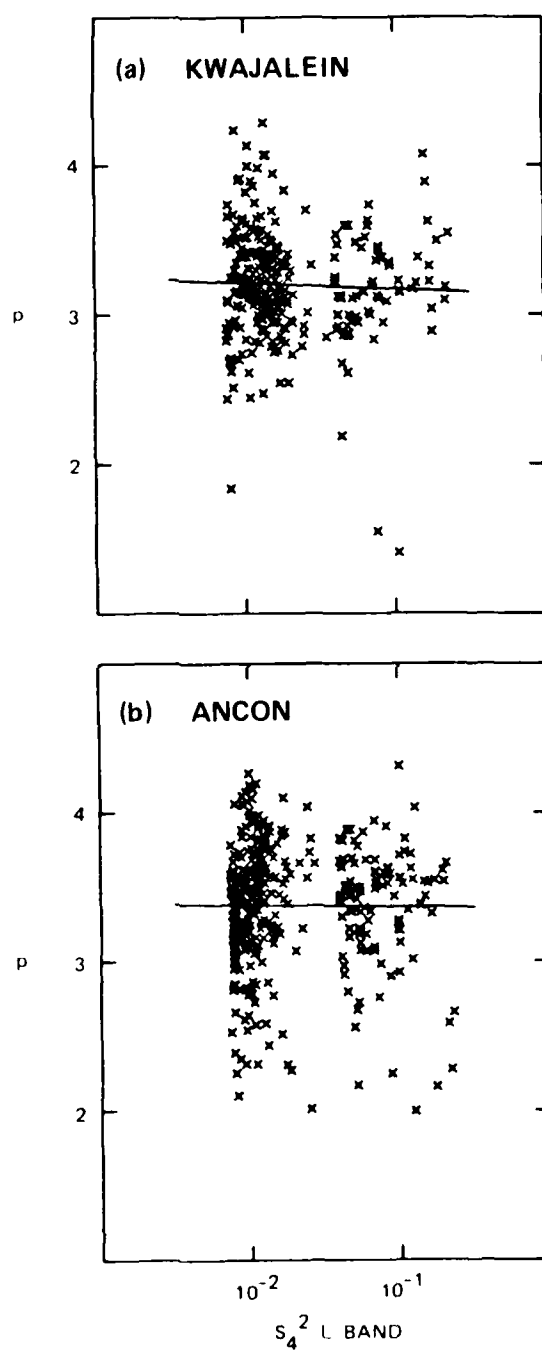


Figure 7. Type 1 spectral index plotted against L-band S_4 .

L-band S_4 value, which as we discussed in Section 1, is proportional to the path-integrated perturbation level.

The Type 2 p_A indices, however, show a distinct decrease in going from UHF to L band. In Figure 8, the individual data points are shown together with the log-linear least-squares fits. Livingston et al. [1981], using in situ satellite data, and Rino et al. [1981a], using in situ rocket data, observed a systematic variation of the in situ spectral index that would manifest itself in the phase spectrum as

$$p_A = p_0 - \eta 10 \log_{10} T , \quad (10)$$

where T is the power-law strength parameter. Their value of $\eta \approx 0.03$ is close to the average values for the two fits shown in Figure 8. Because the break frequencies themselves vary systematically with frequency, however, it is clear that the residual of the diffraction nulls is biasing the breakpoint estimates and the spectral slopes as well. Thus, as discussed in Report I, if we adhere strictly to the weak-scatter criteria, the possibility that the p_A trend in the phase data is a diffraction effect, cannot be excluded.

There is, however, other evidence of a p_A dependence on perturbation strength. From this same data set, Rino and Owen [1982, 1981] showed that by using Eq. (10) the measured coherence time for the strong-scatter VHF data could be brought into excellent agreement with predictions based on the strong-scatter theory. Similarly, in Rino et al. [1981b], it was shown that the behavior of the frequency decorrelation under strong-scatter conditions is also consistent with a varying spectral index. Unfortunately, the strength measures for these analyses were derived from the phase scintillation data rather than from the L-band S_4 index, which is a more robust measure of overall perturbation strength [Rino and Liu, 1982]. Moreover, as discussed in Section 1, recent analyses of high-resolution in situ data from the AE-E satellite do not show the systematic variation that was found in the low-resolution data and in the PLUMEX rocket data [Livingston, private

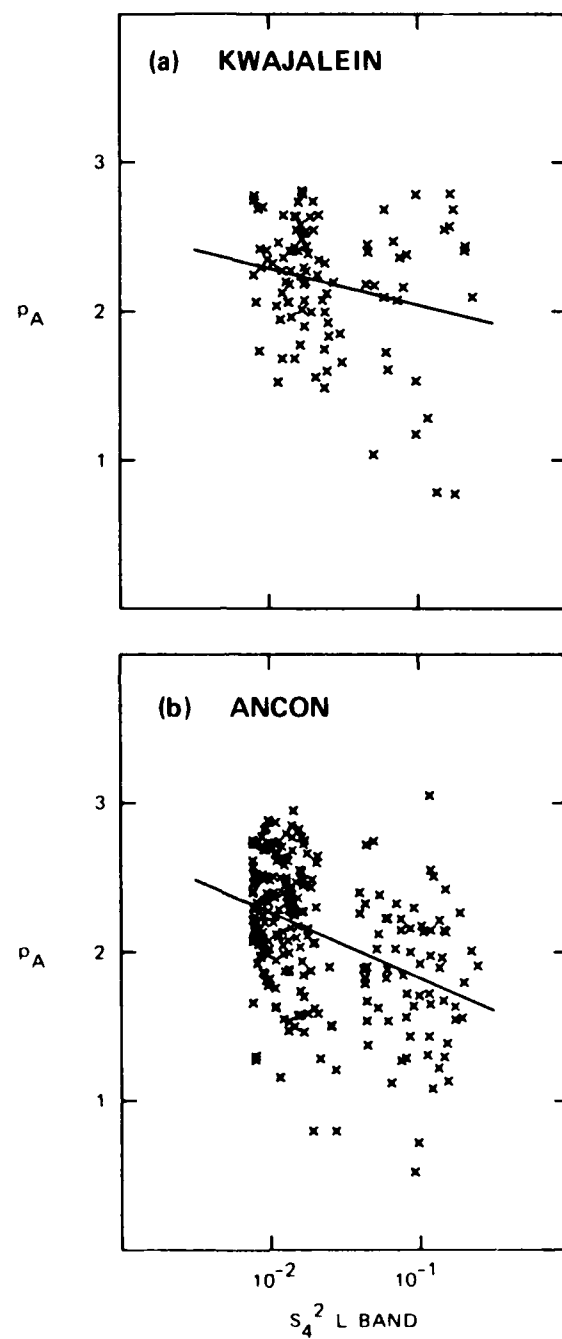


Figure 8. Type 2 p_A spectral index plotted against L-band S_4 .

communication, Rino et al., 1981a]. This suggests that the trend is confined to spatial wavelengths larger than 5 km.

For reference, in Figure 9, we have plotted S_4 and p versus C_s using the thin phase-screen theory for a single-component power law, and the p variation implied by Eq. (10) with an assumed 100-km layer thickness. The plot verifies the nearly linear relation between $\log S_4$ and $\log C_s$ for a single-component power law having a systematically varying spectral index--which is necessary if we are to use S_4 at L band as a measure of absolute integrated perturbation strength. For a two-component power law, a frequency-dependent correction factor must be added that acts to reduce the value of C_s . That is, a given value of C_s will produce a smaller S_4 value than would be inferred from Figure 9; however, in light of the most recent analyses of high resolution AE-E data, this phenomenon clearly needs further study.

2.3 AURORAL-ZONE DATA.

The general morphology of auroral-zone scintillation as measured by the Wideband satellite is described in Rino and Matthews [1980]. Some unique features attributed to the distribution of structure and the anisotropy of the auroral-zone irregularities are described in Fremouw et al., [1977]; Rino et al., [1978]; Rino and Owen, [1980]; and Livingston et al., [1982]. For comparison, we have selected 25 HILAT passes recorded at Tromso, Norway, which has nearly the same invariant latitude as the Wideband station at Poker Flat, Alaska. The HILAT satellite carries a modified version of the Wideband beacon with transmissions at the same VHF and UHF frequencies; however, the L-band signal on HILAT 's used for telemetry and as a phase reference. Thus, no L-band scintillation data are available. The individual passes are summarized in Table 3.

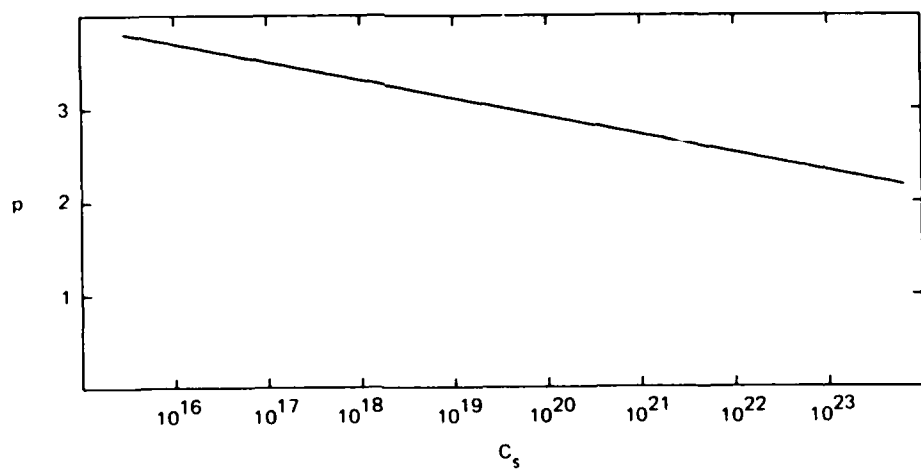
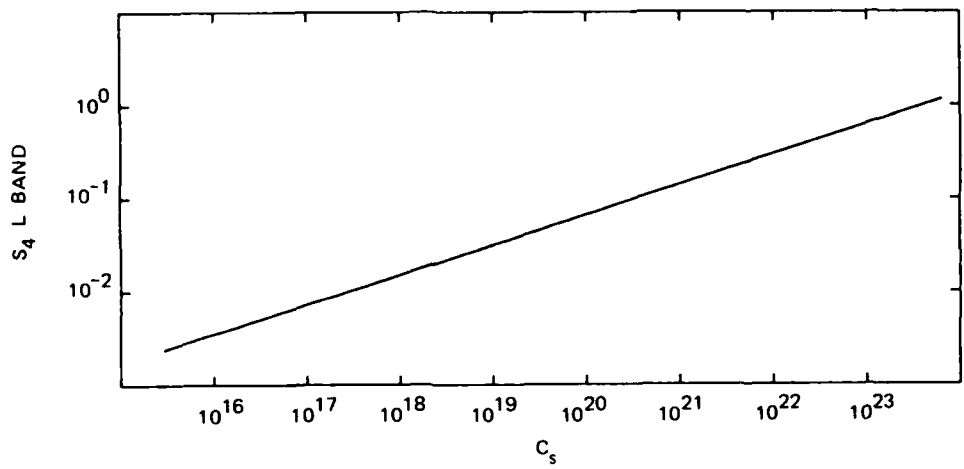


Figure 9. Variation of S_4 and p with C_s as inferred from low-resolution in situ data and corresponding S_4 variation.

Table 3. Summary of auroral-zone passes.

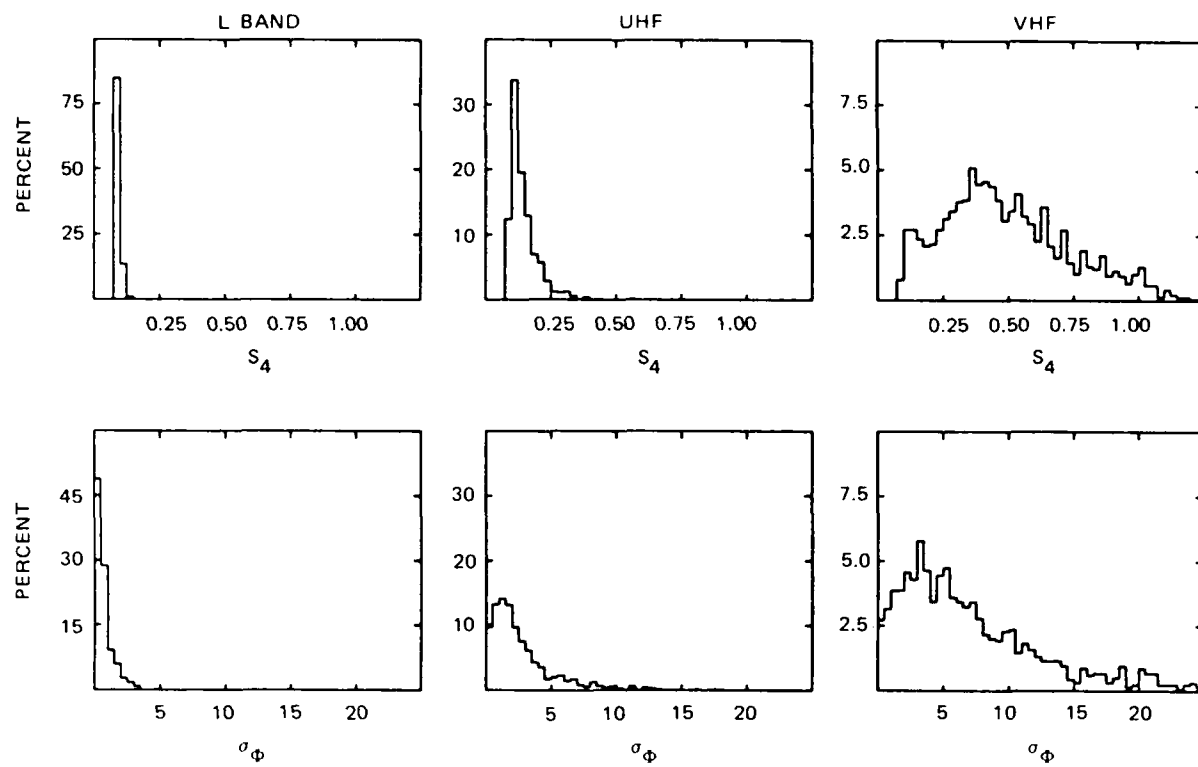
File	Day	Start (UT)	End (UT)	Number of Records
POKER FLAT 1978 (Midnight = 10:00 UT)				
1	59	13:15:02	13:25:17	42
2	60	12:10:27	12:21:57	47
3	61	9:21:22	9:32:52	47
4	61	11:05:42	11:17:12	47
5	61	12:50:02	13:00:47	44
6	62	8:17:03	8:26:18	38
7	62	10:01:02	10:12:32	47
8	62	11:45:22	11:56:52	47
9	62	13:29:32	13:39:32	41
10	63	8:56:22	9:07:22	45
11	63	10:40:42	10:52:12	47
12	63	12:25:05	12:36:20	46
13	64	9:36:02	9:47:32	47
14	64	11:20:22	11:31:52	47
15	68	8:46:02	8:56:47	44
16	68	10:30:22	10:41:52	47
17	82	11:03:53	11:15:23	47
18	82	12:48:13	12:59:13	45
19	86	10:13:54	10:25:24	47
20	86	11:58:14	12:09:44	47
21	88	9:48:53	10:00:23	47
22	88	11:33:13	11:44:43	47
23	88	13:17:23	13:27:53	43
24	99	10:07:43	10:19:13	47
25	99	11:52:13	12:03:43	47
26	102	12:06:48	12:18:18	47
TROMSO 1984 (Midnight = :00 UT)				
1	35	00:43:27	00:53:57	43
2	36	00:17:23	00:27:53	43
3	37	01:33:20	01:43:50	43
4	38	01:07:18	01:17:48	43
5	39	00:41:16	00:51:46	43
6	40	00:15:11	00:25:41	43
7	40	23:49:07	23:59:37	43
8	43	00:39:06	00:49:36	43
9	44	00:13:01	00:23:46	44
10	44	23:46:57	23:57:42	44
11	46	22:54:55	23:05:25	43
12	48	00:10:49	00:21:19	43
13	48	23:44:50	23:55:20	43
14	49	23:18:45	23:29:30	44
15	50	22:52:43	23:03:28	44
16	51	22:26:41	22:37:11	43
17	52	23:42:38	23:53:08	43
18	54	22:50:32	23:01:17	44
19	56	21:58:29	22:08:59	43
20	57	21:32:25	21:43:55	43
21	58	22:48:22	22:58:52	43
22	59	22:22:21	22:32:51	43
23	60	21:56:17	22:07:02	44
24	61	21:30:15	21:40:45	43
25	62	21:04:08	21:14:38	43

The display format is the same as for the equator data. In Figure 10 we show histograms of the occurrence of S_4 and σ_ϕ , and in Figure 11 we show scatter diagrams of the individual measurements. The scintillation levels are much lower than the equator data, so that the UHF and VHF data comprise most of the data that fall within the weak-scatter window. Also, the Tromso station uses a simple helix antenna, whereas a small UHF/L-band dish and a four-element VHF helix array were used with the earlier Wideband data. Thus, the Tromso data admit more noise and multipath contamination. Finally, the Tromso data were recorded near solar minimum, while the earlier Wideband data were recorded during a period of increasing solar activity. In spite of these differences, however, the general occurrence patterns at the two auroral-zone stations are very similar.

Because of the complicated anisotropy of the nighttime auroral-zone irregularities [Livingston et al., 1982], the conversion from temporal to spatial frequency is not as straightforward as it is near the geomagnetic equator, where the diffraction pattern is essentially one-dimensional. Thus, in Figure 12, we show the distributions of v_{eff} for 10:1 rod-like irregularities and 10:5:1 sheet or wing-like irregularities. The orientation of the second irregularity axis is along the local L shell. The differences are significant. We have therefore presented our summary results using two v_{eff} estimates. We note that the Wideband satellite was in a sun-synchronous orbit, whereas the HILAT satellite orbit drifts through 24 hours of local time in 6 months. The geometry of the HILAT passes relative to the local magnetic meridian will vary more than the corresponding geometry of the Wideband satellite passes. Nonetheless, the v_{eff} distributions for 10:5:1 wing-like irregularities are very similar for the two satellites.

Using the same spectral characterization procedure as that used for the Equatorial data, we obtain the distributions shown in Figure 13. No L-band data from the Wideband satellite survive the low S_4 limit, which

(a) POKER FLAT



(b) TROMSO

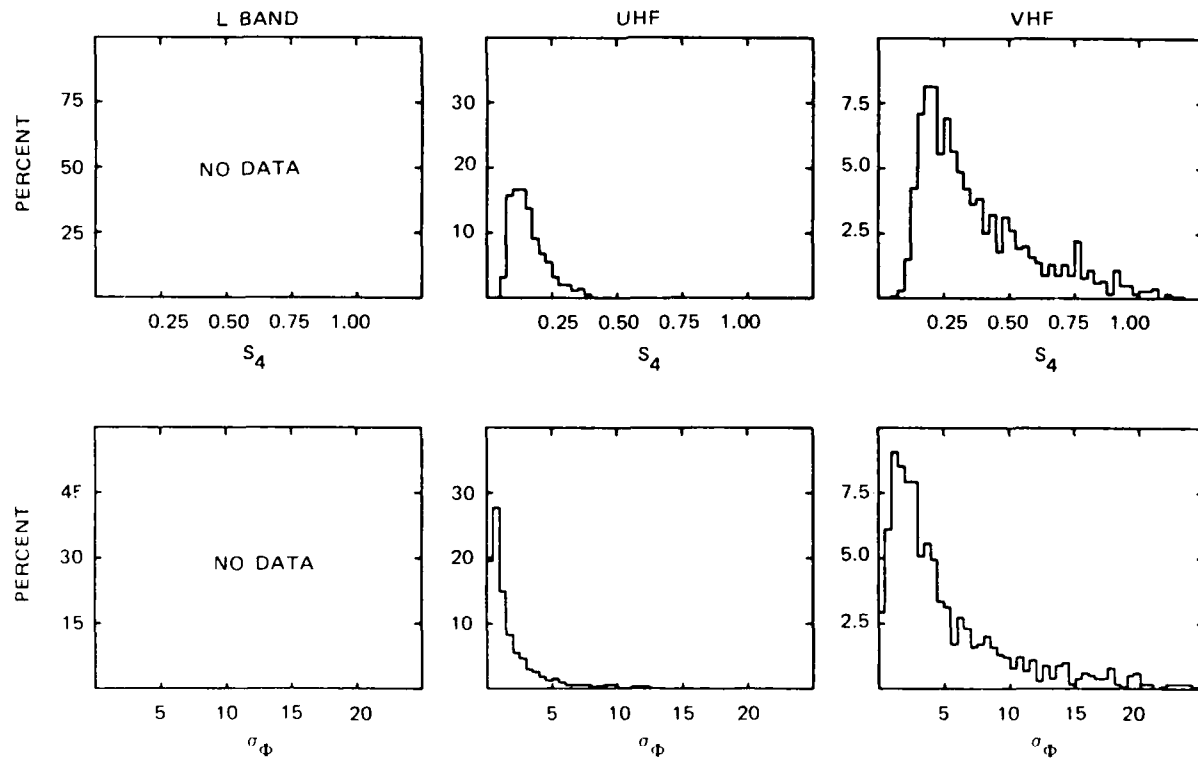


Figure 10. Distributions of auroral-zone intensity and phase scintillation.

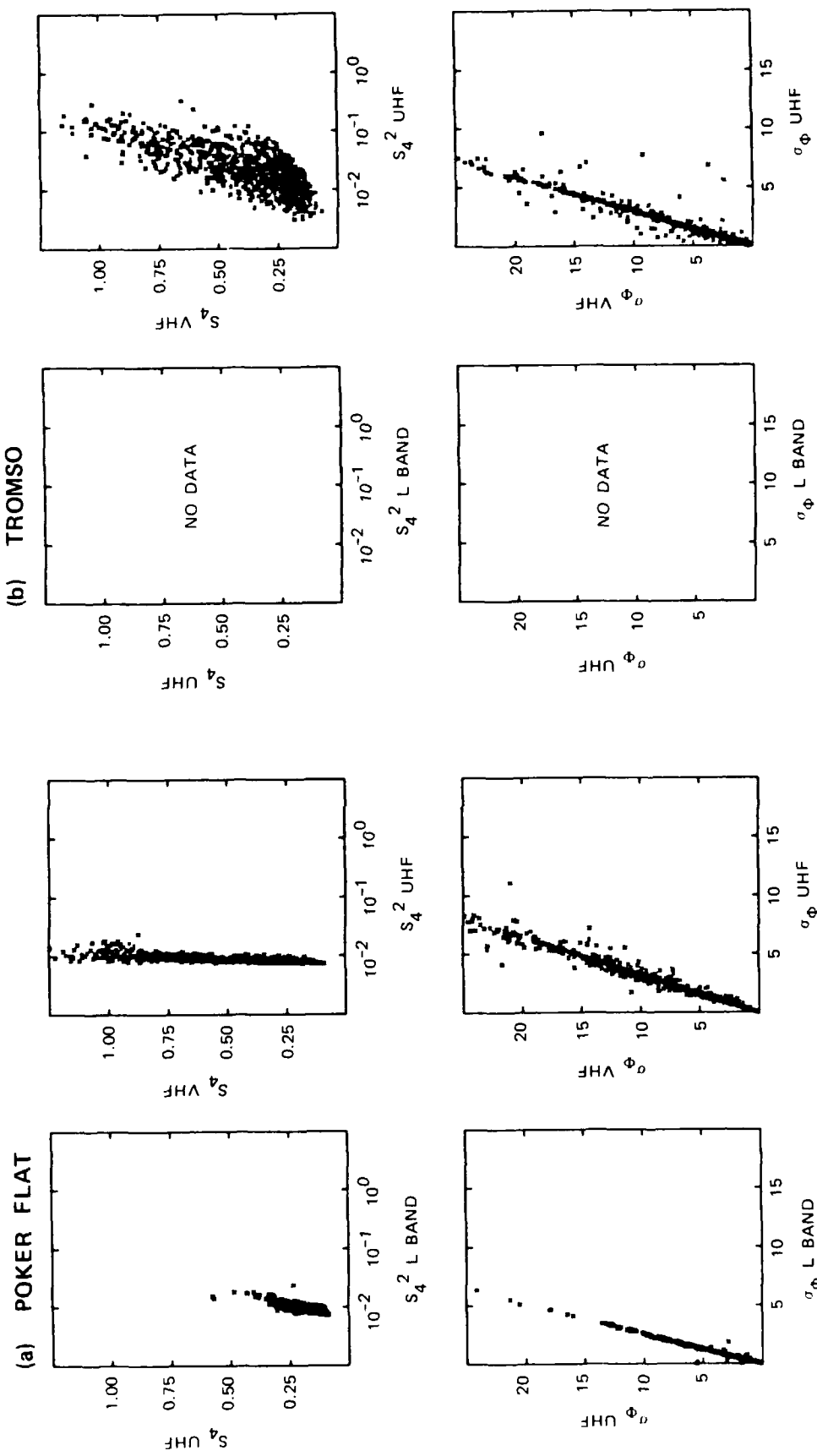


Figure 11. Frequency comparisons of intensity and phase scintillation.

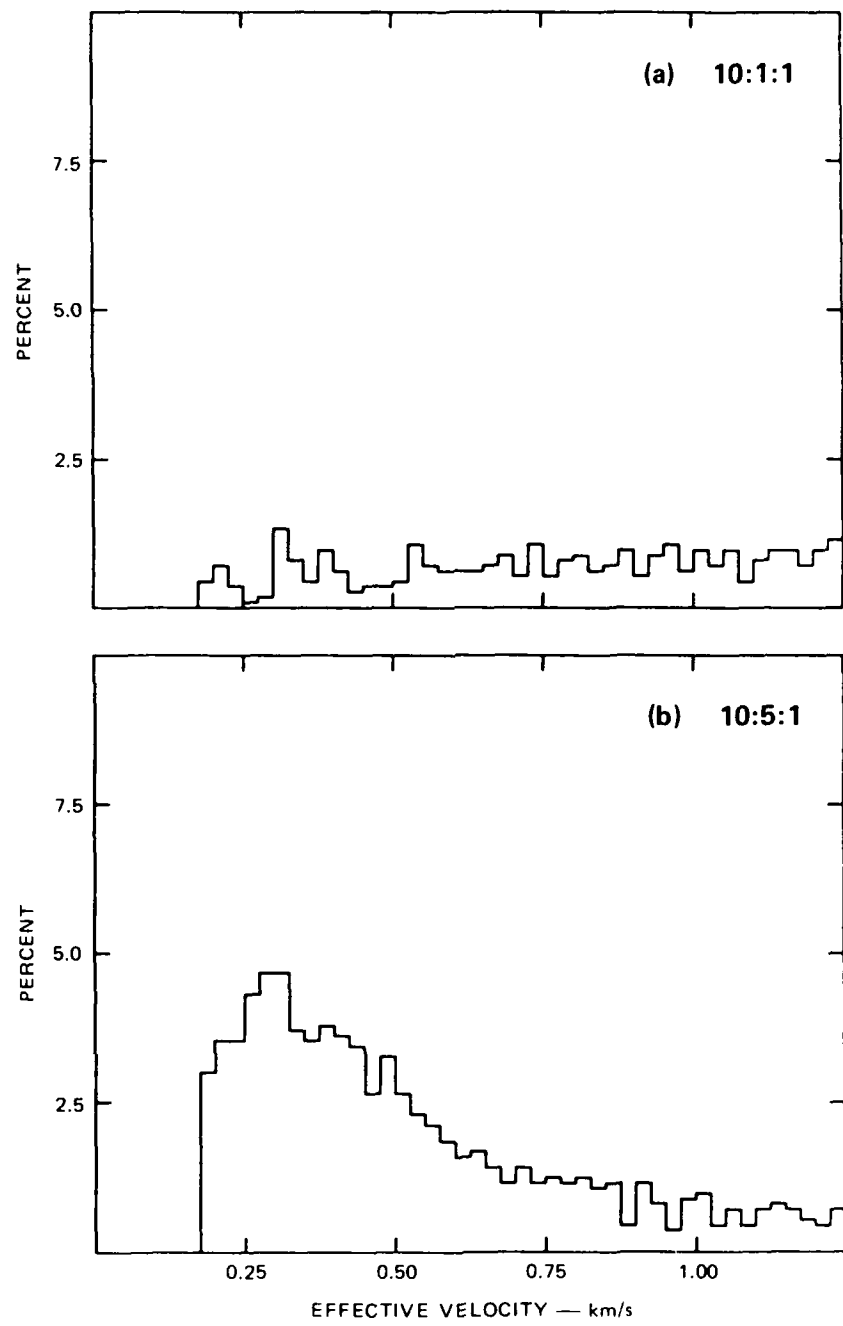


Figure 12(a). Distribution of v_{eff} -- Poker Flat.

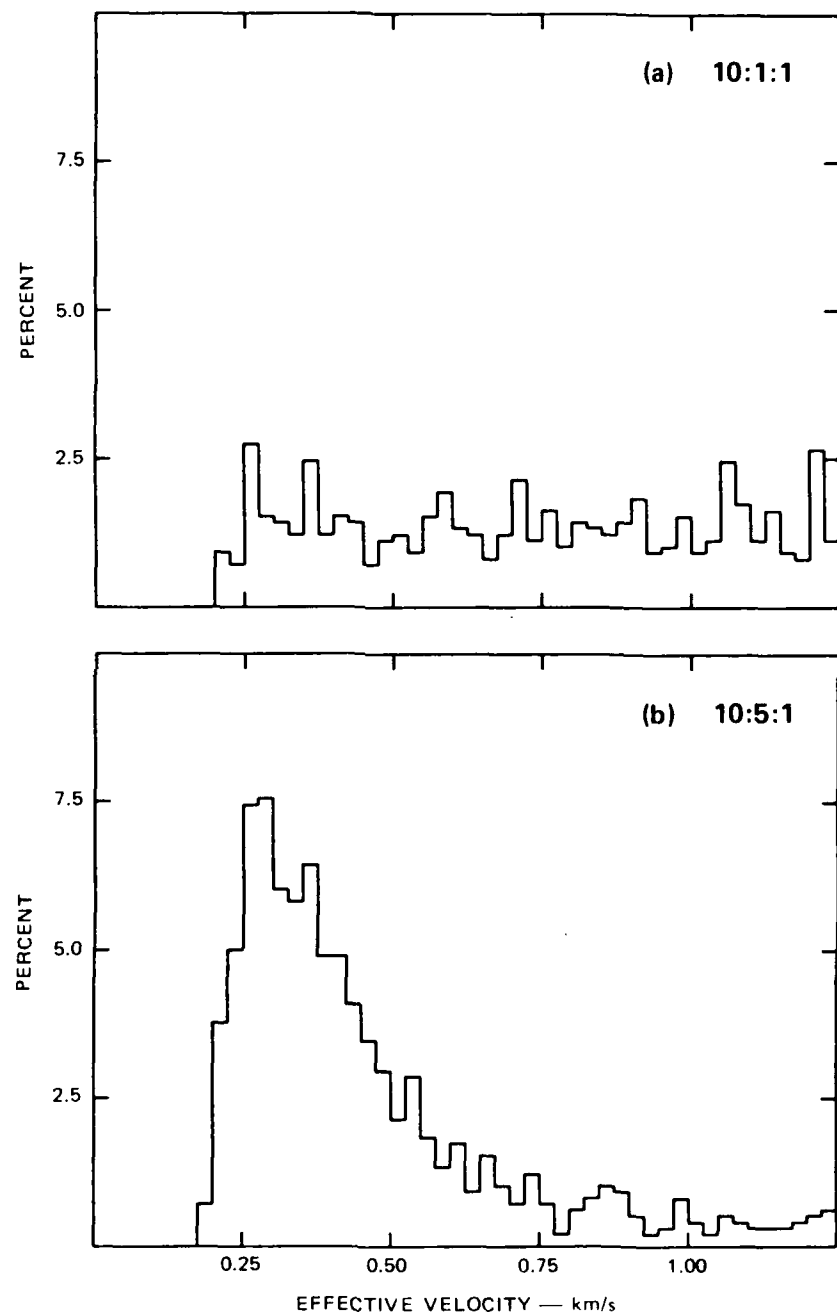


Figure 12(b). Distribution of v_{eff} -- Tromso.

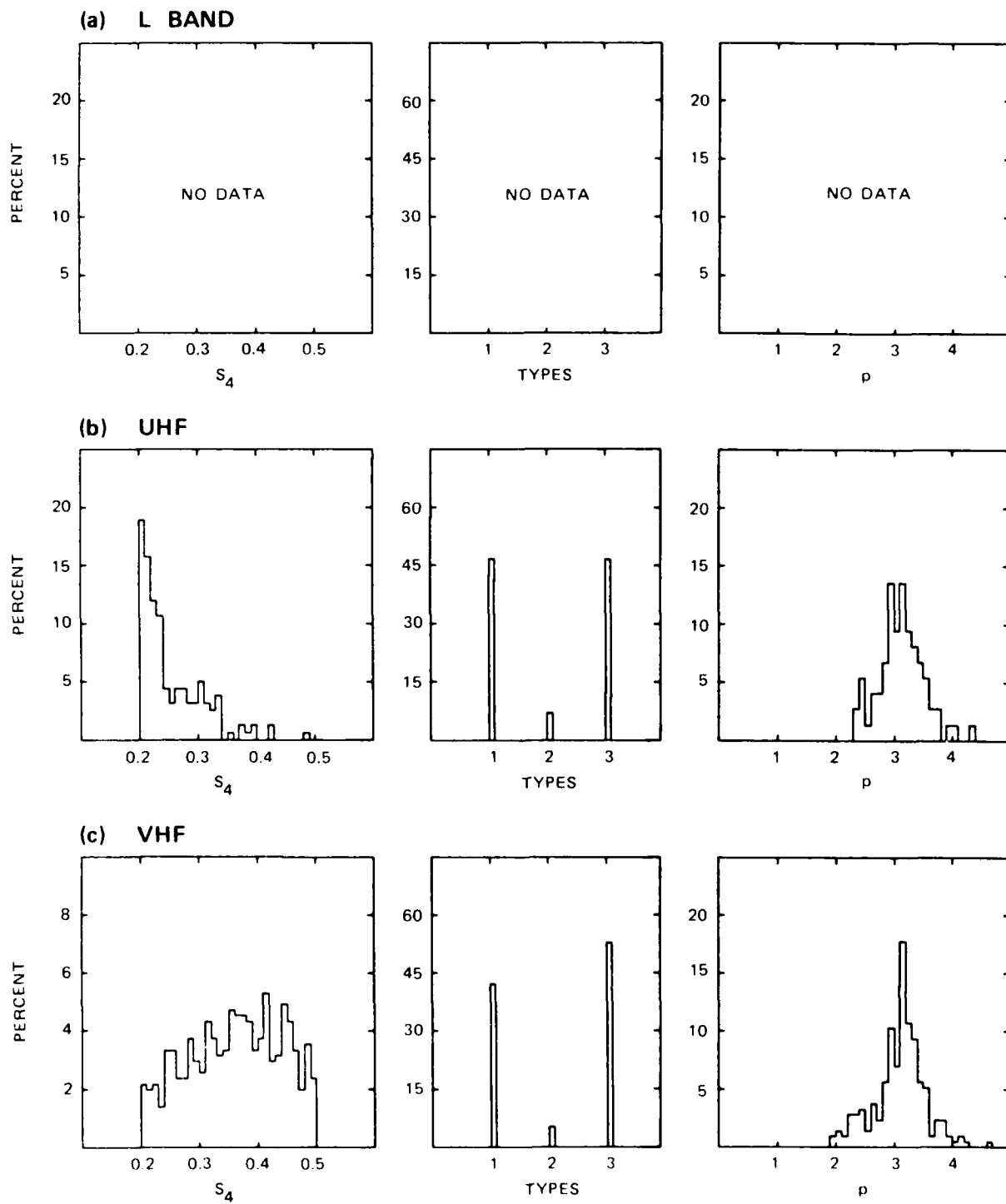


Figure 13(a). Occurrence of spectral types and power-law indices for auroral-zone Type 1 spectra -- Poker Flat.

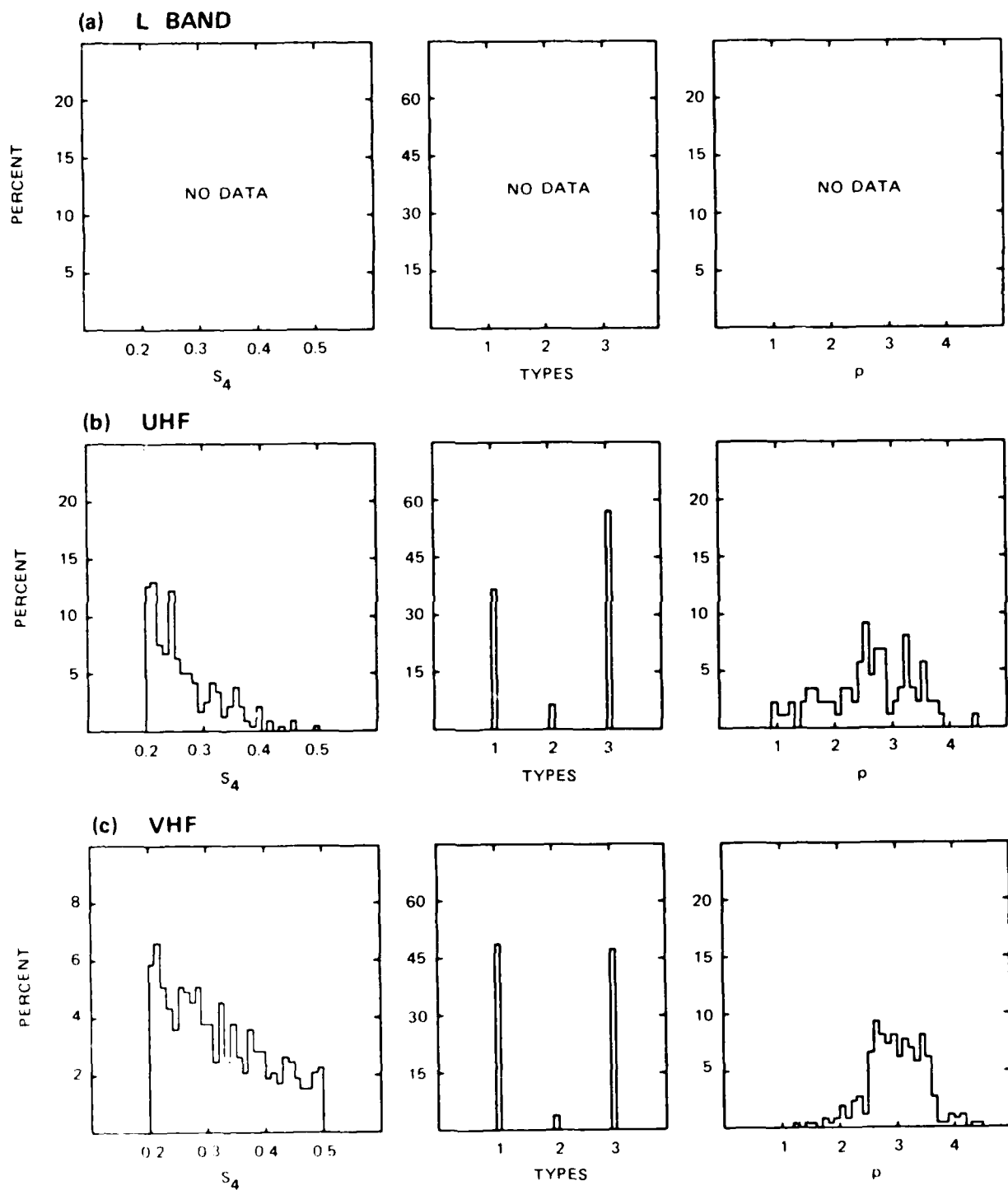


Figure 13(b). Occurrence of spectral types and power-law indices for auroral-zone Type 1 spectra -- Tromso.

is consistent with the generally lower perturbation levels that are characteristic of the auroral zone. Unlike the equator, in the auroral zone, Type 3 spectra with $p_B < p_A$ constitute the dominant two-component configuration. The single-component p indices are slightly shallower than the corresponding population of Equatorial passes, but are otherwise similar. The lower sensitivity of the Tromso data clearly manifests itself in the distribution of p , compared with the corresponding Wideband data, but the general characteristics of the spectra obtained at the two stations are remarkably similar.

Because of the very small number of Type 2 spectra in the auroral zone, the distributions are not well defined, and we have not considered these data further. The Type 3 spectra are summarized in Figure 14. We see that the p_A distributions are virtually identical between the two auroral-zone stations, having a median value between 3 and 4. The steeply-sloped portion of the spectrum extends at least to one kilometer. The variation is due to the different anisotropy models used to infer the actual break point, as discussed above. Measured anisotropy parameters are not available for these data. The high-frequency component of the Type 3 spectra is very shallow with p_B approaching 2; however, the high-frequency ends of the spectra, even in the Poker Flat data, are susceptible to noise contamination at the lower S_4 levels--these results are likely to be biased toward lower values. The general characteristics are consistent at the two stations. The median values are summarized in Table 4.

The shallowly-sloped p_B component of the Type 3 auroral-zone spectra is similar to the shallowly-sloped p_A component found in the equator data at somewhat larger scale sizes and possibly caused by a similar process; however, within the limits of the available data, we cannot establish a perturbation strength dependence of p_B in the auroral-zone. In the earlier analysis of the Wideband satellite data,

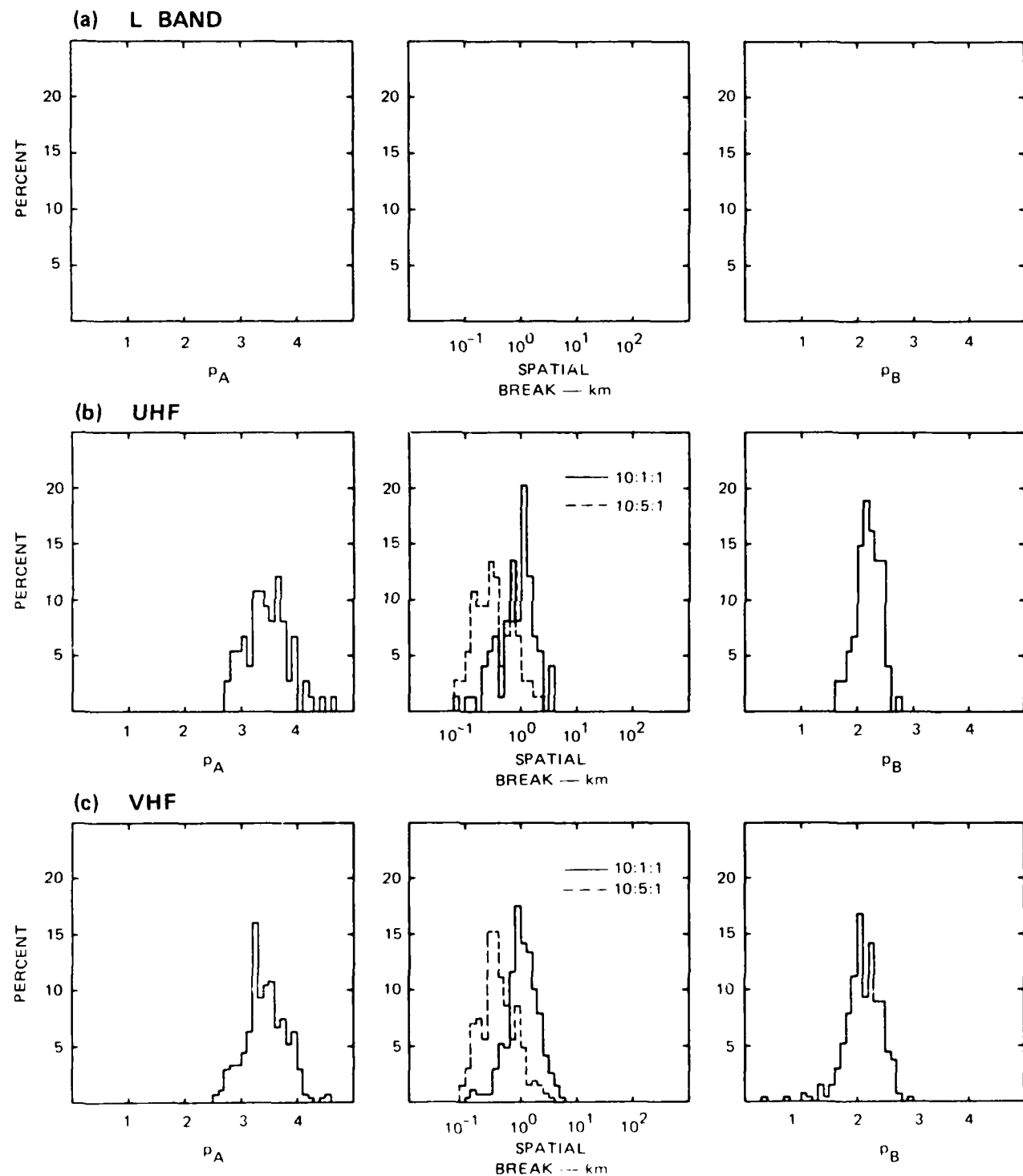


Figure 14(a). Spectral index and break frequency distributions for auroral-zone Type 3 spectra -- Poker Flat.

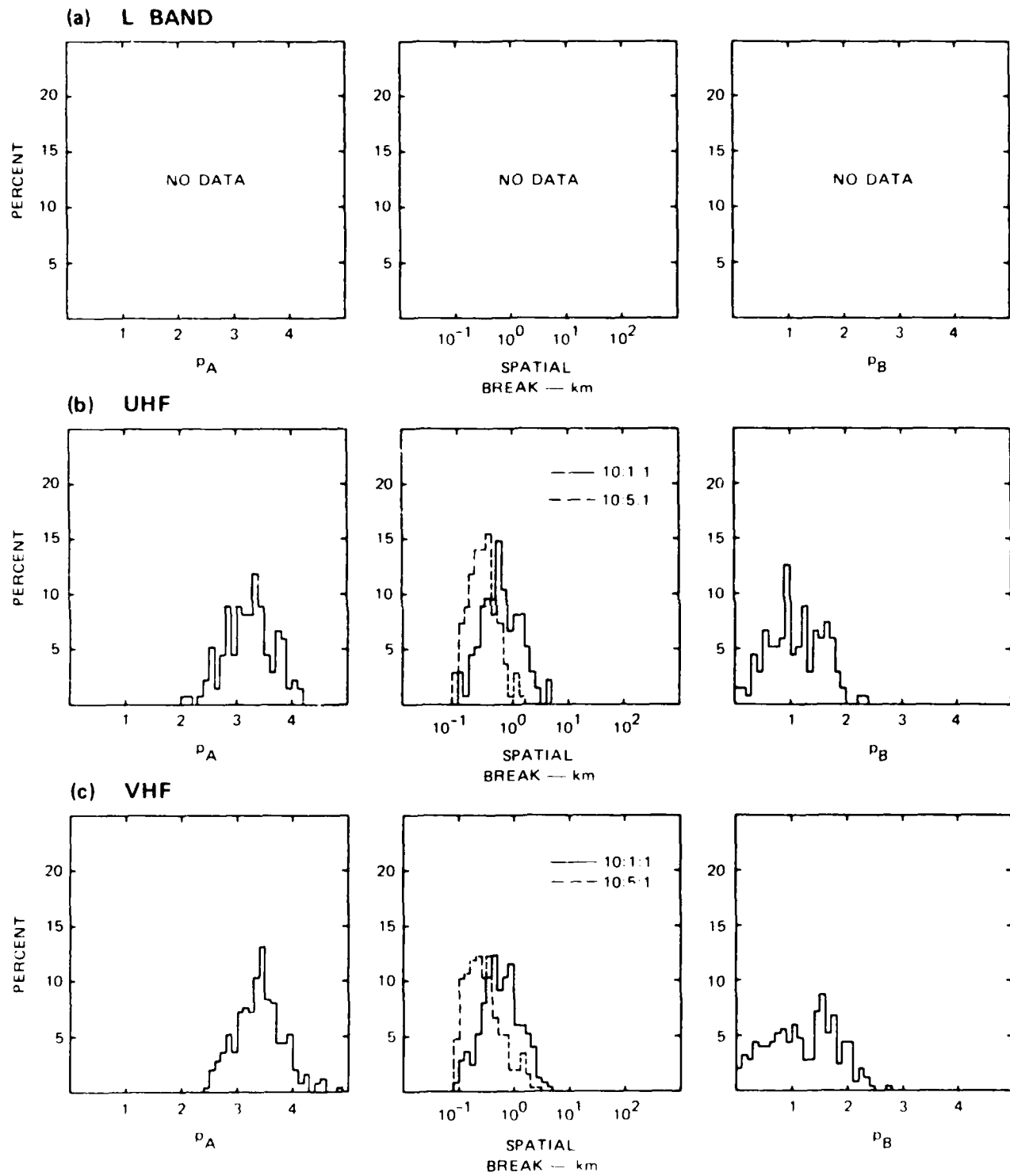


Figure 14(b). Spectral index and break frequency distributions for auroral-zone Type 3 spectra -- Tromso.

Table 4. Summary of auroral-zone spectral characteristics derived using multicomponent curve fitter.

Frequency	Type	No. of Data Samples/Total	Spectral Index	Break (m)	
				10:1:1	10:5:1
POKER FLAT					
VHF	1	214/508	3.10	--	*
UHF	1	74/159	3.12	--	
VHF	2	26/508	--	--	
UHF	2	11/159	--	--	
VHF	3	268/508	3.44, 2.11	1072	912
UHF	3	74/159	3.46, 2.19	813	398
TROMSO					
VHF	1	258/529	2.99	--	
UHF	1	87/237	2.60	--	
VHF	2	201/529	--	--	
UHF	2	15/237	--	--	
VHF	3	251/529	3.39, 1.18	660	309
UHF	3	135/237	3.23, 1.10	708	275

it is almost certain that a combination of the steeply-sloped and more shallowly-sloped spectral components was being measured, but because of the shorter detrend interval, we were still primarily sensitive to the shallowly-sloped component. Thus, our distribution for p_B is shallower than would be expected from the index values we reported in our earlier summaries [Rino, 1979], although, as we have already noted, noise contamination is introducing small biases in the results. Also, Fremouw et al. [1985a] have noted that in the early analysis of the Wideband data detrending without subsequent windowing was used. This allowed enough sidelobe leakage to bias the results toward more shallow values.

To substantiate the general features of the spectral characteristics, we note that processes that are unique to the auroral zone should show a dependence on invariant latitude, most likely controlled by magnetic activity. Thus, in Figure 15 we have plotted the single-component p index values and the p_A and p_B indices for the dominant Type 3 spectra. It can be seen that both the p and the p_A indices tend to decrease with increasing invariant latitude; moreover, because the trend is asymmetric, it is most likely to be a true latitudinal dependence rather than an elevation-angle or magnetic aspect-angle dependence. The corresponding data for p_B , by comparison, show a distinct tendency to form a local maximum at the point where the propagation path intercepts an L shell. This effect has been discussed by Fremouw et al. [1985a], who attribute it to a scale-size dependent anisotropy. The low-frequency enhancement, however, appears to be a genuine auroral-zone characteristic.

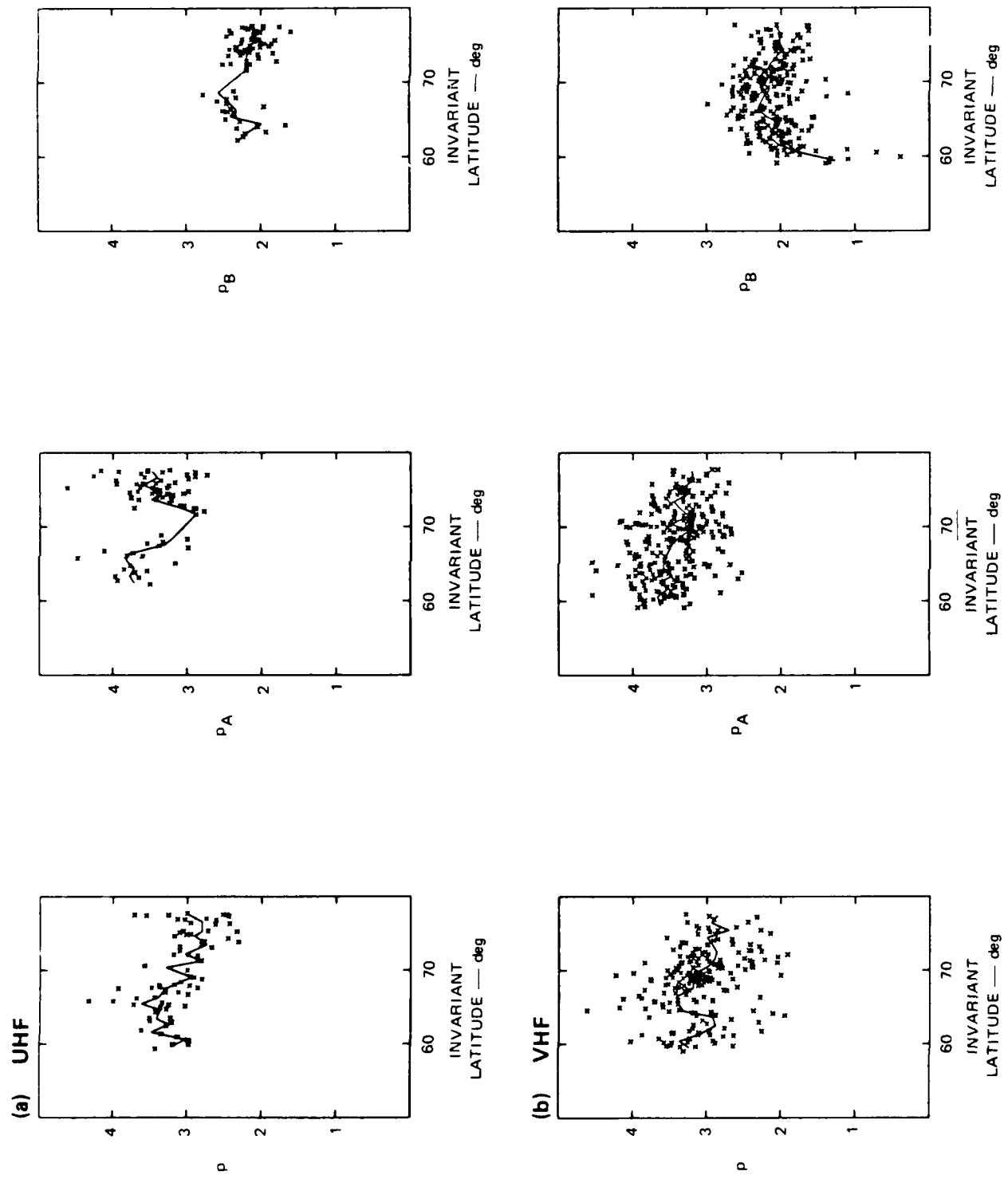


Figure 15(a). Invariant latitude dependence of auroral-zone spectral indices -- Poker Flat, S_4 : 0.2 to 0.5.

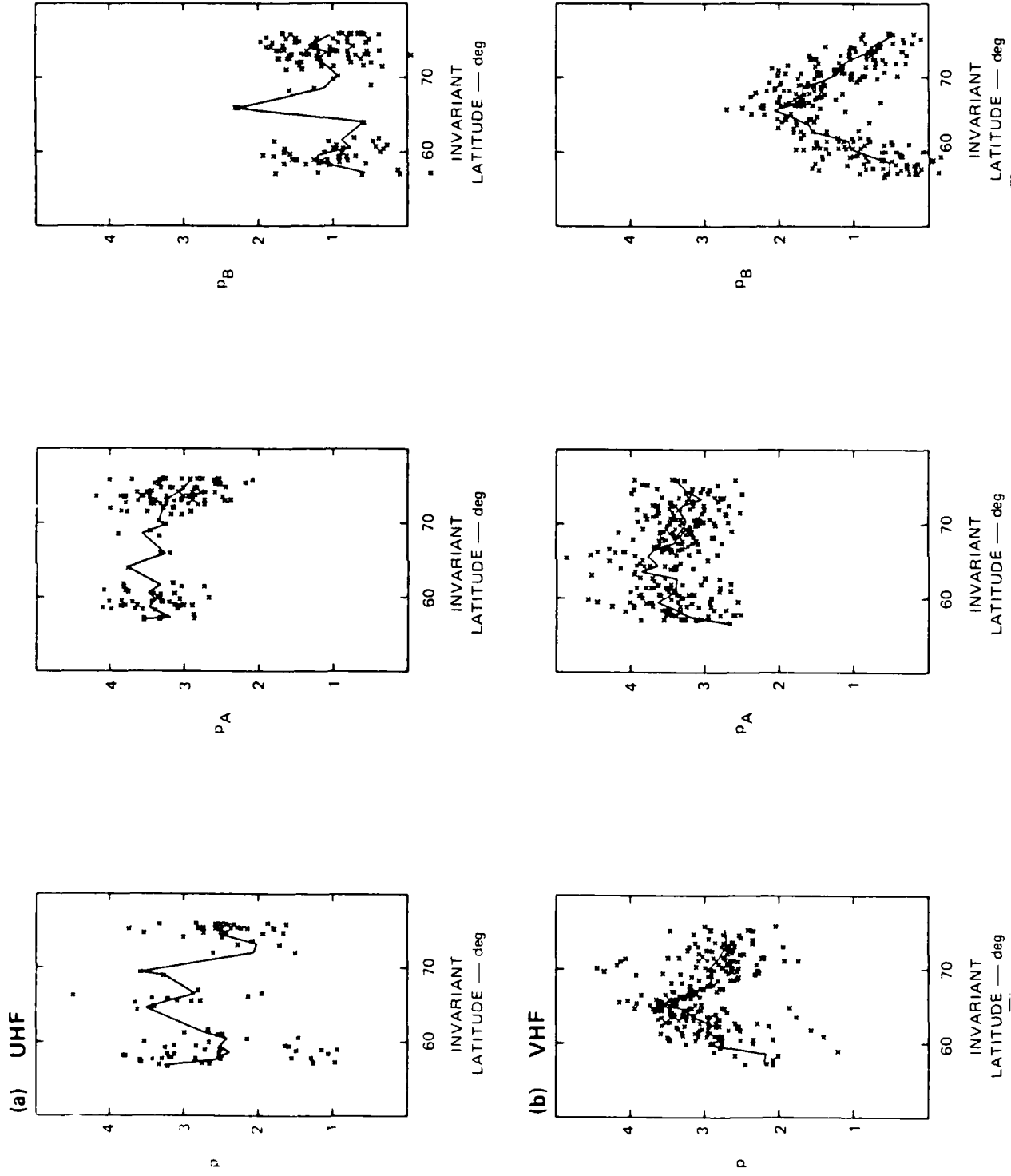


Figure 15(b). Invariant latitude dependence of auroral-zone spectral indices—Tromso, S4: 0.2 to 0.5

SECTION 3

DISCUSSION

The data analysis presented in this paper provides a consistent average spectral characterization of F-region irregularities having scale sizes from a few tens of kilometers to a few hundreds of meters. Within this scale-size regime, equatorial irregularities admit one of two characterizations: (1) single power laws having one-dimensional in situ spectral indices near but somewhat larger than 2, and (2) two-component power laws having intermediate scale indices less than 2 with a transition between 500 and 800 m to power laws more steeply sloped than 2. From the scintillation data alone, we are not able to identify the conditions under which each type occurs; however, in situ rocket probes have shown that the single-component power laws are observed primarily in bottom-side structures [Keskinen et al., 1981] and within or on the walls of large depletions [Rino et al., 1981a; Kelley, et al., 1982; Kelley et al., 1986; LaBelle and Kelley, 1986]. In situ satellite probes, which scan the structures horizontally rather than vertically, seem to be in agreement with this occurrence pattern of single-component and two-component spectra [Livingston, private communication].

The single-component spectra having one-dimensional in situ indices near 2 agree with the predictions of both theory and numerical simulations of the gravity-driven Rayleigh-Taylor instability [Ossakow, 1979; Keskinen et al., 1981]; however, as noted by Kelley et al. [1986], the two-component spectra remain largely unexplained. LaBelle et al. [1986] have reviewed two hypotheses that can possibly explain the two-component spectra. One hypothesis assumes that the structure is caused by two-dimensional turbulence in the velocity field, which can give rise to a two-component spectrum in connection with a reverse cascade of energy (from small- to large-scale sizes), and a downward cascade of enstrophy

(vorticity variance) that conserves two invariants. This mechanism was originally proposed by Kraichnan [1967]; it has been observed in neutral turbulence [Lilly, 1983] and has been demonstrated in numerical simulations of "guiding-center plasmas" by Seyler et al. [1975]. As reviewed in Kintner and Seyler [1985], however, the application of the theory relies on a passive scalar relation between density and velocity (collisionless structuring) and it implicitly requires an isotropic velocity field. We believe that these restrictions are too severe and that alternate hypotheses must be considered.

We had suggested an alternative hypothesis, which is discussed in LaBelle et al. [1986]. Batchelor [1959] showed that highly anisotropic structures in a passive scalar field give rise to a k^{-1} spectrum. Batchelor was studying passive scalar turbulence beyond the viscous cut-off in the velocity field where strong linear shears are known to develop. We noted that a very similar structure occurs in the velocity field of the highly anisotropic evolution of convective instabilities. The irregularities are drawn out along the direction of the average cross-field drift, which may be caused by any combination of electric fields, gravity, or neutral winds. The results show that a very shallowly-sloped intermediate-scale regime is indeed associated with the highly anisotropic structure evolution in purely collisional instabilities; however, the results also suggest that the anisotropy is scale-size dependent. In any case, the two-component model itself seems to be well supported by a variety of independent data--if not yet fully explained.

Regarding the steeply-sloped transition-scale regime, the spectral indices derived from the phase scintillation data give results significantly shallower than values reported from in situ measurements and even intensity scintillation data [Kelley et al., 1982; Franke and Liu, 1983]. As discussed in Report I, it is possible that the diffraction-induced rapid phase changes are yet biasing the data. Indeed, diffraction effects in phase tend to become larger as the scale sizes decrease, whereas intensity spectra are affected very differently and would tend

to give a steeper result than is measured in situ. Also, at sufficiently small scale sizes, temporal rearrangement of the structure during the measurement can also bias or smear the result. In any case, it is clear that the steepened portion of the spectrum is a manifestation of enhanced diffusion-like processes that are rapidly eroding the steep gradients that would otherwise result from the natural evolution of convective structuring.

Turning to the auroral-zone data, the existence of a low-frequency spectral enhancement in the Wideband satellite data had been noted by Fremouw et al., [1985a]; however, the usual practice of fitting linear segments over fixed temporal-frequency regimes seems to have obscured the persistence of this feature. Indeed, as with the equatorial Type 2 spectra, the occurrence of auroral-zone Type 3 spectra is remarkably consistent over time and auroral-zone location. Auroral-zone irregularities have been reviewed by Fejer and Kelley [1980], Kelley et al., [1982], Vickrey and Kelley [1982], and Tsunoda [1986], who discussed a general framework for the production, convection, and dissipation of auroral-zone irregularities. They emphasized the connection of the high-latitude F region to the distant magnetosphere and to a highly conducting E region, which can provide direct sources of irregularities through structured velocity fields and precipitating particles, and can profoundly influence the evolution of such structures.

It is possible that the low-frequency component of the two-component spectra is a manifestation of direct velocity stirring--as suggested by Vickrey and Kelley [1982]. Once established, convective instabilities would sustain a continued structure enhancement. In this context, the patchiness of high-latitude scintillation would be attributed to electrodynamic processes that cause structuring on a scale of tens to hundreds of kilometers [Robinson et al., 1985; Tsunoda et al., 1985; Tsunoda, 1986]. Fremouw et al., [1985a] have suggested that the sheet-like anisotropy observed in the night-side auroral-zone scintillation data is also caused by the direct deposition of structure. With strong zonal convection, the structures would presumably be imparted

with a configuration close to the form toward which any east-west gradient would tend to evolve, as discussed by Vickrey and Kelly [1982].

The source of the more shallowly-sloped component beyond one kilometer is puzzling. The scale sizes are small enough that diffusion should be acting to steepen the spectrum. We note that Villain et al. [1986] report a steepening of in situ spectra beyond a few hundred meters. This suggests that the shallowly-sloped portion at the high-frequency end of the spectrum might well be caused by the same mechanism that causes shallowly-sloped spectra in the equatorial zone, but extending to somewhat smaller scale sizes. The vastly different geometries causing variations along (rather than across) field lines could possibly account for such effects. Finally, we note that Basu et al. [1984] have observed shallow-sloped in situ spectra to occur in the vicinity of strong velocity shears and have suggested a cause-effect relation. All the analyses performed to date, however, show that inertial effects alone are either stabilizing or that they evolve structure at a much slower rate than purely collisional mechanisms [Satyanayana and Ossakow, 1984; Mitchell et al., 1985; Keskinen et al., 1986].

Ultimately, a consistent explanation of the results will require a better understanding of how intermediate-scale structures evolve, and particularly how this evolution manifests itself in the measurable one-dimensional spectral characteristics. Tsunoda [1986] has developed a unified framework within which the auroral-zone structure enhancement can be interpreted. However, much of the observed differences between the equatorial and auroral-zone structures, may yet be explainable by the different geometries or, simply, by the different conductivity ratios.

As was described in Report I, the propagation results reported here must ultimately be extrapolated to predict the nuclear disturbed environment. The first link in that extrapolation procedure involves verifying that the phase spectral shapes reflect the in situ density structure.

This can only be done by conducting an analysis similar to this one on in situ measurements. Such an effort is currently underway for Atmosphere Explorer equatorial data. We intend, under continued DNA support, to analyze high-latitude in situ data as well. In addition to verifying the spectral shapes, these studies will emphasize the physics that control the different shapes observed. It is only through a detailed understanding of these underlying physical processes that the extrapolation to the nuclear regime can be done with confidence.

SECTION 4

LIST OF REFERENCES

Basu, S., and S. Basu, "High-Resolution Topside in situ Data of Electron Densities and VHF/GHz Scintillations in the Equatorial Region," J. Geophys. Res., Vol. 88, No. A1, pp. 403-415 (January 1983).

Basu, S., S. Basu, E. MacKenzie, W. R. Coley, W. B. Hanson, and C. S. Lin, "F-Region Electron Density Irregularity Spectra Near Auroral Acceleration and Shear Regions," J. Geophys. Res., Vol. 89, No. A7, pp. 5554-5564 (July 1984).

Batchelor, G. K., "Small-Scale Variation of Convected Quantities Like Temperature in Turbulent Fluid--Part 1. General Discussion and the Case of Small Conductivity," J. Fluid Mech., Vol. 113, p. 113 (1959).

Bhattacharyya, A., and R. G. Rastogi, "Phase Scintillations due to Equatorial F-Region Irregularities with Two-Component Power-Law Spectrum," Radio Sci., Vol. 20, No. 4, pp. 935-946, July-August (1985).

Crane, R. K., "Spectra of Ionospheric Scintillation," J. Geophys. Res., Vol. 81, No. 13, pp. 2041-2050 (May 1976).

Fejer, B. G., and M. C. Kelley, "Ionospheric Irregularities," Rev. Geophys. and Space Phys., Vol. 18, No. 2, pp. 401-454 (May 1980).

Franke, S. J., and C. H. Liu, "Observations and Modeling of Multi-Frequency VHF and GHz Scintillations in the Equatorial Region," J. Geophys. Res., Vol. 88, No. A9, pp. 7075-7085 (September 1983).

Fremouw, E. J., "Geometrical Control of the Ratio of Intensity and Phase Scintillation Indices," J. Atmos. Ter. Phys., Vol. 42, pp. 775-782 (September/October 1980).

Fremouw, E. J., and R. E. Robins, "An Equatorial Scintillation Model," Technical Report DNA-TR-85-333, Contract DNA001-83-C-0097, Physical Dynamics, Inc., Bellevue, Washington (September 1985).

Fremouw, E. J., J. A. Secan, and J. M. Lansinger, "Spectral Behavior of Phase Scintillation in the Nighttime Auroral Region," Radio Sci., Vol. 20, No. 4, pp. 923-933 (1985a).

Fremouw, E. J., C. L. Rino, R. C. Livingston, and M. C. Cousins, "A Persistent Subauroral Scintillation Enhancement Observed in Alaska," Geophys. Res. Lett., Vol. 4, pp. 539-542 (1977).

Fremouw, E. J., R. L. Leadabrand, R. C. Livingston, M. D. Cousins, C. L. Rino, B. C. Fair, and R. A. Long, "Early Results from the DNA Wideband Satellite Experiment--Complex-Signal Scintillation," Radio Sci., Vol. 13, No. 1, pp. 167-187 (1978).

Jakeman, E., "Fresnel Scattering by a Corrugated Random Surface with Fractal Slope," J. Opt. Soc. Am., Vol. 72, No. 8, pp. 1034-1041 (August 1982).

Kelley, M. C., J. F. Vickrey, C. W. Carlson, and R. Torbert, "On the Origin and Spatial Extent of High-Latitude F Region Irregularities," J. Geophys. Res., Vol. 87, No. A6, pp. 4469-4475 (June 1982).

Kelley, M. C., R. C. Livingston, C. L. Rino, and R. T. Tsunoda, "The Vertical Wave-Number Spectrum of Topside Equatorial Spread F: Estimates of Backscatter Levels and Implications for a Unified Theory," J. Geophys. Res., Vol. 87, No. A7, pp. 5217-5221 (July 1982).

Kelley, M. C., J. LaBelle, E. Kudeki, B. G. Fejer, S. Basu, S. Basu, K. D. Baker, C. Hanuise, P. Argo, R. F. Woodman, W. E. Swartz, D. T. Farley, and J. W. Meriwether, Jr., "The Condor Equatorial Spread F Campaign: Overview and Results of the Large-Scale Measurements," J. Geophys. Res., Vol. 91, No. A5, pp. 5487-5503 (May 1986).

Keskinen, M. J., E. P. Szuszczewicz, S. L. Ossakow, and J. C. Holmes, "Nonlinear Theory and Experimental Observations of the Local Collisional Rayleigh-Taylor Instability in a Descending Equatorial Spread F Ionosphere," J. Geophys. Res., Vol. 86, No. A7, pp. 5785-5792 (July 1981).

Keskinen, M. J., J. Fedder, S. Zalesak, J. Huba, H. Mitchell, and P. Satyanarayana, "Nonlinear Evolution of the Kelvin-Helmholtz Instability in the High-Latitude Ionosphere," NRL Memo Report, Naval Research Laboratory, Washington, D.C. (1986).

Kintner, P. M., and C. E. Seyler, "The Status of Observations and Theory of High Latitude Ionospheric and Magnetospheric Plasma Turbulence," Space Sci. Rev., Vol. 41, pp. 91-129 (1985).

Kraichnan, R. H., "Inertial Ranges in Two-Dimensional Turbulence," Physics of Fluids, Vol. 10, No. 7, p. 1417 (July 1967).

LaBelle, J., and M. C. Kelley, "The Generation of Kilometer Scale Irregularities in Equatorial Spread F," J. Geophys. Res., Vol. 91, No. A5, pp. 5504-5512, 1986.

LaBelle, J., M. C. Kelley, and C. E. Seyler, "An Analysis of the Role of Drift Waves in Equatorial Spread F," J. Geophys. Res., Vol. 91, No. A5, pp. 5513-5525 (May 1986).

Lilly, D. K., "Stratified Turbulence and the Mesoscale Variability of the Atmosphere," J. Atmos. Sci., Vol. 40, p. 749 (1983).

Livingston, R. C., "Comparison of Multifrequency Equatorial Scintillation: American and Pacific Sectors," Radio Sci., Vol. 15, No. 4, pp. 801-814 (July-August 1980).

Livingston, R. C., C. L. Rino, J. P. McClure, and W. B. Hanson, "Spectral Characteristics of Medium-scale Equatorial F Region Irregularities," J. Geophys. Res., Vol. 86, No. A4, pp. 2421-2428 (April 1981).

Livingston, R. C., C. L. Rino, J. Owen, and R. T. Tsunoda, "The Anisotropy of High-Latitude Nighttime F Region Irregularities," J. Geophys. Res., Vol. 87, No. A12, pp. 10,519-10,526 (December 1982).

Livingston, R. C., private communication, 1986.

Livingston, R. C., and T. M. Dabbs, "Phase Scintillation Under Weak and Strong Scatter Conditions," DNA Technical Report, Contract DNA 001-85-C-0062, SRI International, Menlo Park, California (submitted for review September 1986).

Mitchell, H. G., Jr., J. A. Fedder, M. J. Keskinen, and S. T. Zalesak, "A Simulation of High-Latitude F-layer Instabilities in the Presence of Magnetosphere-Ionosphere Coupling," Geophys. Res. Lett., Vol. 12, No. 5, pp. 283-286 (May 1985).

Ossakow, S. L., "Ionospheric Irregularities," Rev. of Geophys. and Space Phys., Vol. 17, No. 4, pp. 521-533 (1979).

Rino, C. L., "A Power-Law Phase Screen Model for Ionospheric Scintillation, I. Weak Scatter," Radio Sci., Vol. 14, No. 6, pp. 1135-1145 (1979).

Rino, C. L., "On the Application of Phase Screen Models to the Interpretation of Ionospheric Scintillation Data," Radio Sci., Vol. 17, No. 4, pp. 855-867 (1982).

Rino, C. L., and C. H. Liu, "Intensity Scintillation Parameters for Characterizing Transionospheric Radio Signals," Radio Sci., Vol. 17, No. 1, pp. 279-284 (1982).

Rino, C. L., and S. J. Matthews, "On the Morphology of Auroral-Zone Radiowave Scintillation," J. Geophys. Res., Vol. 85, No. A8, pp. 4139-4151 (1980).

Rino, C. L., and J. Owen, "The Structure of Localized Nighttime Auroral Zone Scintillation Enhancements," J. Geophys. Res., Vol. 85, No. A6, pp. 2941-2948 (June 1980).

Rino, C. L., and J. Owen, "On the Temporal Coherence Loss of Strongly Scintillating Signals," Radio Sci., Vol. 16, No. 1, pp. 31-33 (January-February 1981).

Rino, C. L., and J. Owen, "The Mutual Coherence Function for Trans-ionospheric Radio Waves," Radio Sci., Vol. 17, No. 3, pp. 675-683 (1982).

Rino, C. L., and J. Owen, "Numerical Simulations of Intensity Scintillation Using the Power Law Phase Screen Model," Radio Sci., Vol. 19, No. 3, pp. 891-908 (1984).

Rino, C. L., R. C. Livingston, and S. J. Matthews, "Evidence for Sheet-like Auroral Ionospheric Irregularities," Geophys. Res. Lett., Vol. 5, No. 12, pp. 1029-1042 (December 1978).

Rino, C. L., R. T. Tsunoda, J. Petriceks, R. C. Livingston, M. C. Kelley, and K. D. Baker, "Simultaneous Rocket-Borne Beacon and In Situ Measurements of Equatorial Spread F--Intermediate Wavelength Results," J. Geophys. Res., Vol. 86, No. A4, pp. 2411-2420 (1981a).

Rino, C. L., V. H. Gonzalez, and A. R. Hessing, "Coherence Bandwidth Loss in Transitionospheric Radio Propagation," Radio Sci., Vol. 16, No. 2, pp. 245-255 (March-April 1981b).

Robinson, R. M., R. T. Tsunoda, J. F. Vickrey, and L. Guerin, "Sources of F-Region Ionization Enhancements in the Nighttime Auroral Zone," J. Geophys. Res., Vol. 90, No. A8, pp. 7533-7546 (August 1985).

Satyanarayana, P., and S. L. Ossakow, "Velocity Shear Stabilization of the Current Convective Instability," J. Geophys. Res., Vol. 89, No. A5, pp. 3019-3022 (May 1984).

Secan, J. A., and E. J. Fremouw, "Improvement of the Scintillation-Irregularity Model in WBMOD," Final Report DNA-TR-81-241, Contract DNA001-81-C-0092, Physical Dynamics, Inc., Bellevue, Washington (February 1983).

Seyler, C. E., Y. Salu, D. Montgomery, and G. Knorr, "Two-Dimensional Turbulence in Inviscid Fluids or Guiding Center Plasmas," Phys. of Fluids, Vol. 18, No. 7, pp. 803-813 (July 1975).

Tsunoda, R. T., "High-Latitude F-Region Irregularities: A Review and Synthesis," DNA Technical Report, Contract DNA 001-86-C-0002, Menlo Park, California (1986).

Tsunoda, R. T., I. Haggstrom, A. Pellinen-Wannberg, A. Steen, and G. Wannberg, "Direct Evidence of Plasma Density Structuring in the Auroral F Region Ionosphere," Radio Sci., Vol. 20, No. 4, p. 762 (July-August 1985).

Vickrey, J. F., and M. C. Kelley, "Irregularities and Instabilities in the Auroral F Region," High-Latitude Space Plasma Physics, Plenum, New York (1982).

Villain, J. P., C. Beghin, and C. Hanuise, "ARCAD3-SAFARI Coordinated Study of Auroral and Polar F-Region Ionospheric Irregularities," Ann. Geophys., Vol. 4, pp. 61-68 (1986).

Wittwer, L., private communication, 1986.

Yeh, K. C., and C. H. Liu, "Radio Wave Scintillations in the Ionosphere," Proc. IEEE, Vol. 70, No. 4, pp. 324-360 (1982).

APPENDIX

AN ALGORITHM FOR SEGMENTED LINEAR-CURVE FITS*

A.1 INTRODUCTION.

We have developed an automated procedure for making multisegmented fits to functional data. In the past, it was necessary to fit linear segments to data by making linear least-squares fits to specific regions of the data. The ranges for the linear fits are preselected or the linear regions in the data are determined by observing each data set individually. While the former method is very efficient, it is subjective; furthermore, it cannot be used if the linear regions are non-stationary. The latter method, while objective, is very time consuming, thus, it cannot be used to analyze a large data set. The new algorithm combines objectivity with efficiency; it is a superior method for sorting data into linear regimes. In this Appendix, we describe the method and its usage; then we explain the details of the algorithm.

A.2 PHILOSOPHY.

Like the method of least squares, our scheme approximates the dependence of one variable on another. Both methods describe the relationship analytically. The method of least squares finds a polynomial representation of the form

$$F(x) = A_N * x^{n-1} + A_{N-1} * x^{n-2} + \dots + A_2 * x^1 + A_1 . \quad (A.1)$$

* This Appendix has been prepared by Teri M. Dabbs

Our scheme finds a multisegmented representation of the form

$$\begin{aligned} F(X) &= M_1 * X + B_1 \quad , \quad X_1 < X < X_2, \\ &= M_2 * X + B_2 \quad , \quad X_2 < X < X_3, \\ &\quad \cdot \\ &\quad \cdot \\ &= M_{n-1} * X + B_{n-1}, \quad X_{n-1} < X < X_n . \end{aligned} \tag{A.2}$$

Although the two methods describe the relationship between two variables in a similar fashion, each representation has its own advantages and disadvantages. We developed the multisegmented fitting scheme to compensate for the shortcomings in the method of least squares. To be specific, we wanted a scheme that would fit two-dimensional data with the flexibility of a high-order-polynomial fit, and that would give results that are as simple to interpret as a linear fit.

Every two-dimensional data set can be accurately represented by some high-order polynomial; when the degree of the polynomial fit is one less than the number of data points, the polynomial can represent the data exactly. Unfortunately, the significant structure in the data is not directly inferred from the high-order-polynomial fits. Although the continuous changes in the polynomial can be found indirectly by differentiating the equation, the local trends are still unavailable; thus, comparisons between polynomials are complicated and difficult to comprehend. In contrast, the trend in a segment is obvious from its linear equation. The slope of the line defines the trend in the data over the range of the segment. Because the slope of the segment measures the trend in the data, comparisons between segments are direct and simple to understand.

Although linear fits are easy to interpret, they will not accurately represent trends in complicated data. They will hide significant structure in data when their range covers two or more distinct regions.

For example, the data in Figure 16 have two distinct regions. For $X < 0$, the values of Y are increasing; for $X > 0$, the values of Y are decreasing. A linear least-squares fit approximates the data by the linear equation $F(X) = 0.5 * X + 1.0$. The slope of the line, 0.5, shows a positive dependence of Y on X . The two significant trends have been averaged. If the ranges of the two trends could be defined, the trends could be separated by making a linear fit to each regime. For instance, if we made two linear fits to the data in Figure 16, a fit less than zero and another fit greater than zero, we would measure the two trends. The first region would be approximated by the equation

$$F(X) = 2.0 * X + 5.0 ,$$

and the second region would be approximated by the equation

$$F(X) = -1.0 * X + 5.0 .$$

The two slopes, 2 and -1, accurately describe the relationship between X and Y for the two regions.

Clearly, when we know the ranges of the linear regions in the data, we can give a simple and accurate description by making linear least-squares fits to each linear regime. Unfortunately, we do not always know their ranges. The linear regions can be randomly varying--they can move around in the data. For example, the spectra of phase scintillation data admit both random and systematic variations. A beacon on a satellite transmits radio frequencies that measure phase scintillation. Because the geometry of the satellite pass changes the effective speed of the satellite through the ionosphere, the relationship between the spatial domain and the frequency domain changes.

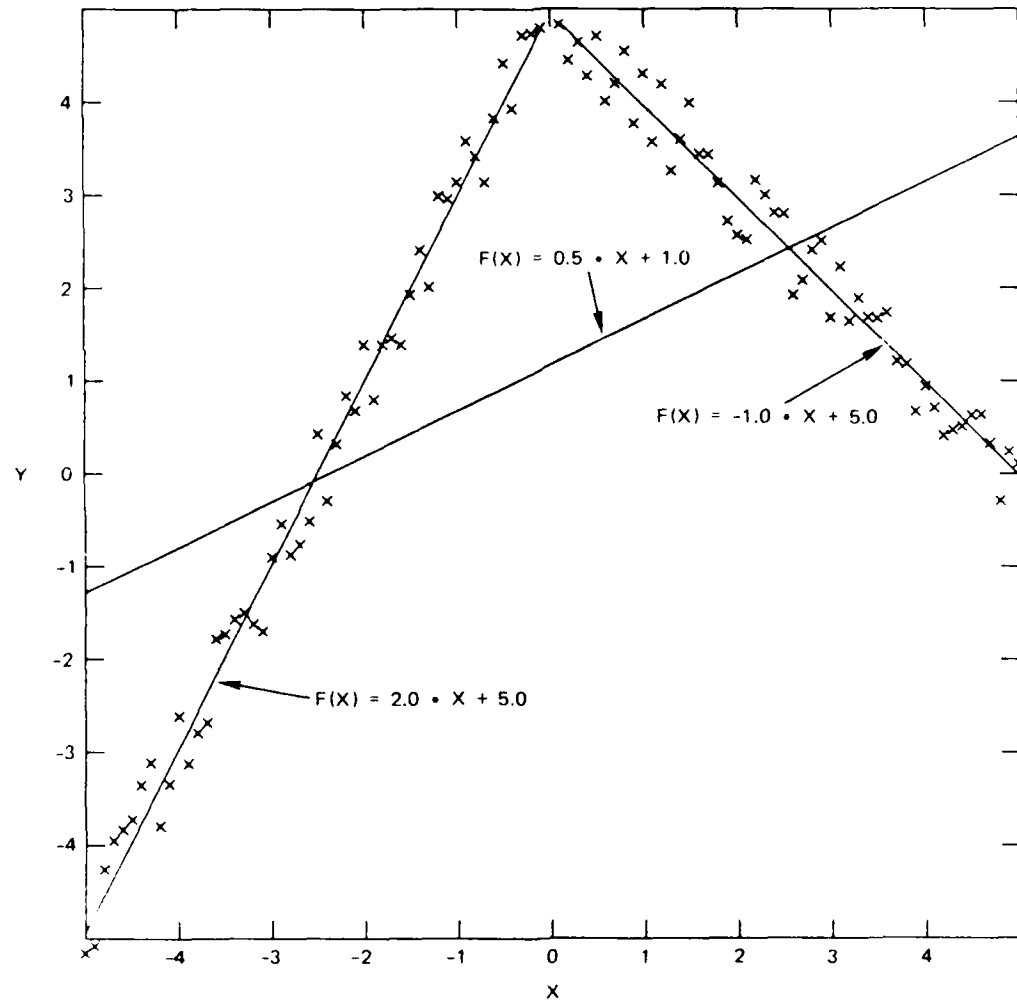


Figure 16. Linear fit versus multisegment fit.

Assuming the linear regions in the phase scintillation data are defined spatially, we know their positions in frequency will vary; therefore, we cannot define the ranges of the linear regions in terms of the frequency.

Because we cannot always preselect the linear regions in functional data, we developed a scheme that uses the data to find their own linear regimes. By predicting the ranges of the linear regions, we are able to make multisegmented fits. These fits are simple to interpret and they give an accurate description of the data. This method can be used whenever a least-squares polynomial fit would be an appropriate approximation to the data. We use this scheme to sort the data into linear regimes, when the ranges of the linear regions cannot be predetermined.

A.3 DESCRIPTION OF MULTISEGMENTED FITTING PROCEDURE.

By observing that different people tend to find the same linear segments in data when they are presented in a rectangular graph, we concluded that the linear regimes are selected objectively and systematically. Furthermore, we believed that an algorithm could emulate this process. By decomposing this abstract visual experience into simple tasks, we developed a logical procedure for finding linear trends in two-dimensional data. The resulting algorithm consists of finding the overall trend, determining the linear regions, then finding the linear equations that represent each region.

We find the overall trend by making a least-squares polynomial fit to the data, then evaluating the polynomial at the end points. The line containing these two points mathematically defines the overall trend--it describes the change in the dependent variable over the range of the independent variable. We have not attempted to make this scheme general enough to determine the ideal degree of the polynomial fit; instead, we let the person using this scheme choose the degree of the fit. The polynomial should be flexible enough to bend with the significant trends

in the data; thus, the degree of the polynomial should be greater than or equal to the number of linear regimes. Figure 17 shows this trend.

From the polynomial fit and the overall trend, we estimate the linear regions, i.e., the regions of the polynomial that are monotonically increasing or decreasing relative to the overall trend. The end points of each linear region have a unique relationship to the overall trend. At these points, the tangent to the polynomial is parallel to the overall trend. In mathematical terms, let

F = least-squares polynomial fit to the data

F' = derivative of least-squares polynomial fit to the data

Slope = slope of line defining overall trend.

We find the points within the range of the data where

$F' = \text{slope}$.

That is, we find the solutions to the following equation,

$F' - \text{slope} = 0$.

The degree of the equation determines the maximum number of solutions to this equation. Because we are using these solutions to separate the data into increasing and decreasing regions, we are only interested in the solutions that occur between the end points. The mean value theorem ensures that at least one solution will occur in this range. Using the end points and the solutions between them, we define the regions in the polynomial that are monotonic relative to the overall trend. Because data are discrete rather than continuous, we must check that these monotonic regions are definable. When the degree of a polynomial fit is

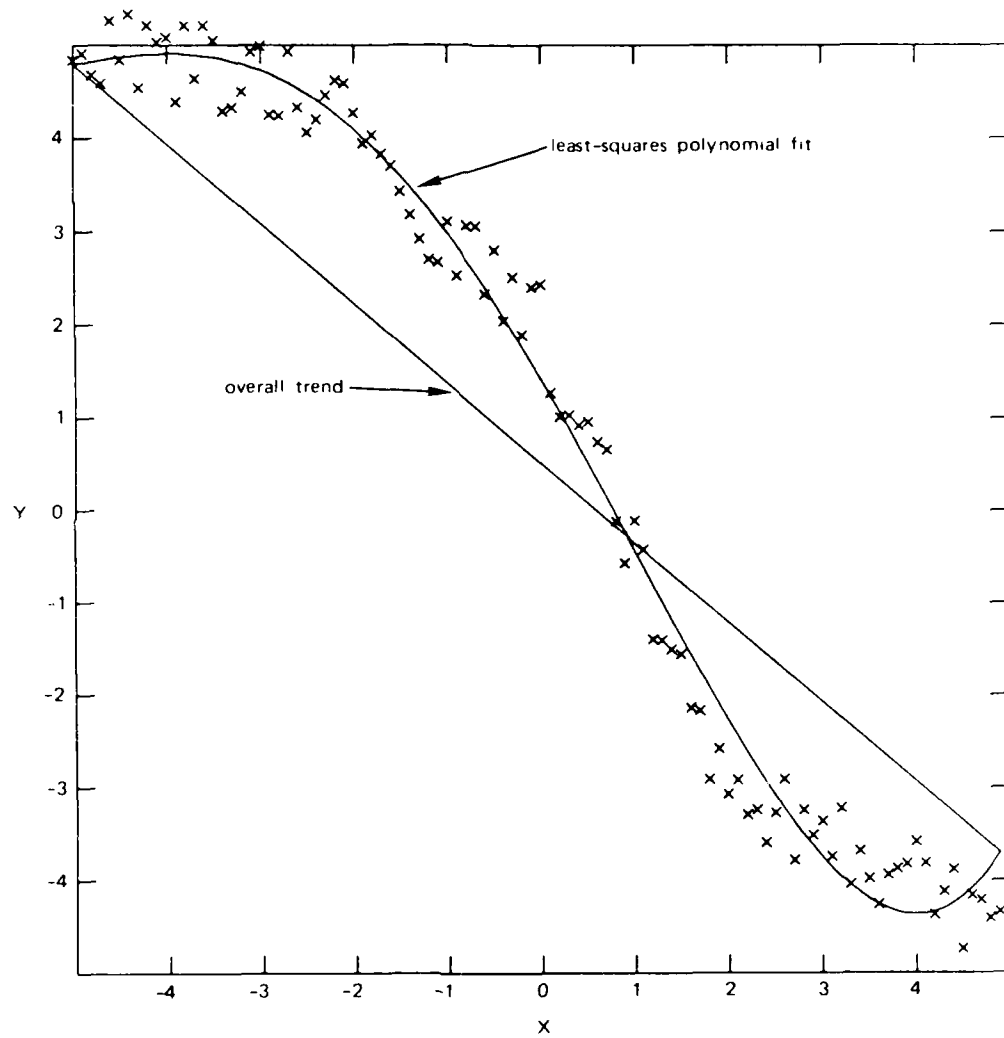


Figure 17. Overall trend determined from least-squares polynomial fit.

higher than the data require, the polynomial can make bends between two consecutive data points. These bends are meaningless; they do not represent the data. Again, we have not attempted to make this scheme general enough to determine the number of data points that would make a region significant. Because a segment cannot be defined without two distinct points, each region must contain at least two data points; however, the person who uses this scheme may define a more stringent requirement.

If any region does not meet this criterion, we make a new polynomial fit to the data. The degree of the new polynomial fit is one less than the previous fit; thus, the new fit is less flexible. We repeat the entire process until we find monotonic regions in the polynomial that are representative of the data. Figure 18 shows the points that estimate the linear regions in the data. Notice that the tangents to the polynomial at these points are parallel to the overall trend.

After predicting the linear ranges in the data, we refine our estimates by making linear least-squares fits to each regime. If the data are well-behaved, we make the linear fits to the original data points; otherwise, we make the fits to the polynomial representation of the data. Figure 19 illustrates the linear fits to the original data points over each region, and Figure 20 illustrates the linear fits to the polynomial representations. Although the fits to the original data points are more representative of the data, these fits can be adversely affected by stray data points. From these linear fits we redefine the ranges of each linear region. We determine the corrected range of each region by finding the intersection of the lines representing consecutive regions. Figures 21 and 22 show the final segment fits to the data, and to the polynomial representation of the data, respectively. Although Figure 21 is a better fit, both fits emphasize the major trends.

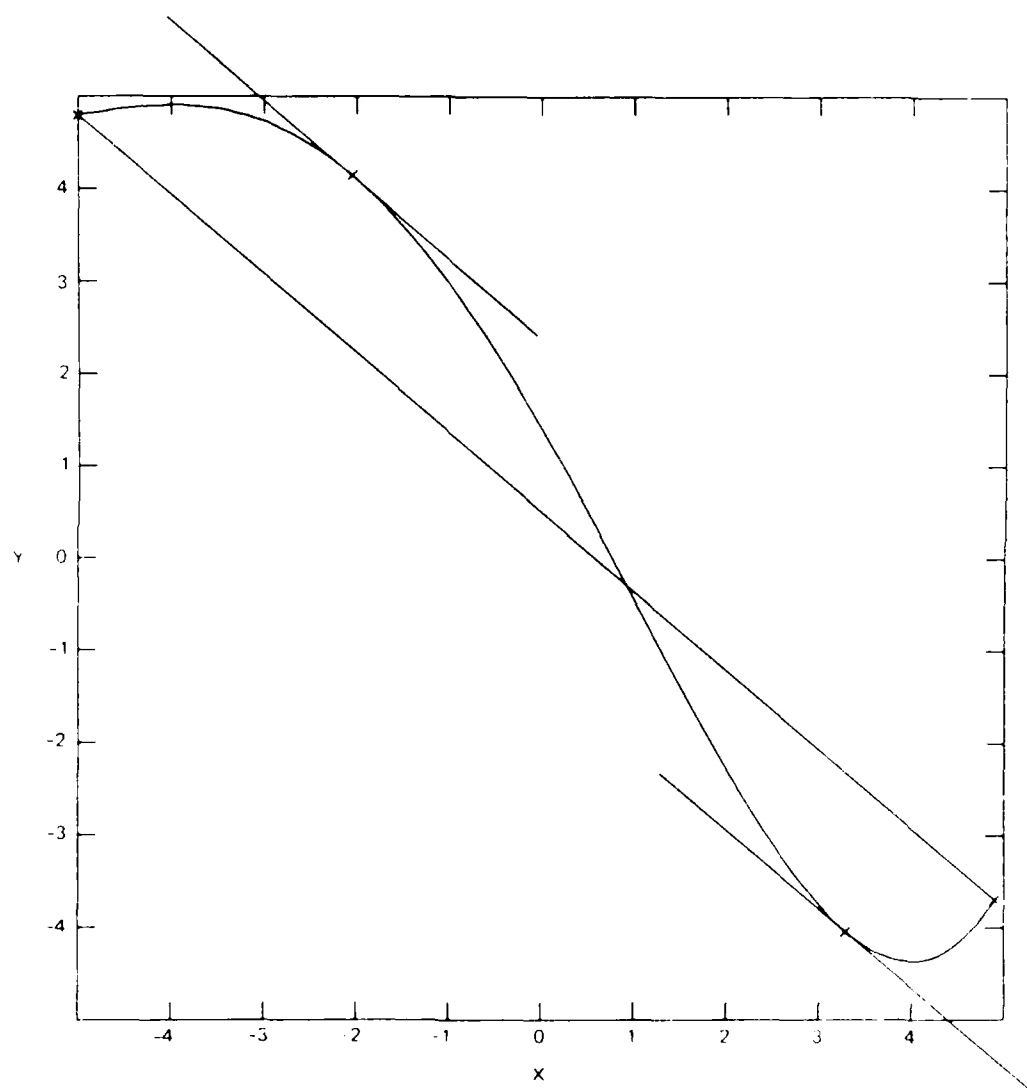


Figure 18. Tangents to polynomial that are parallel to overall trend.

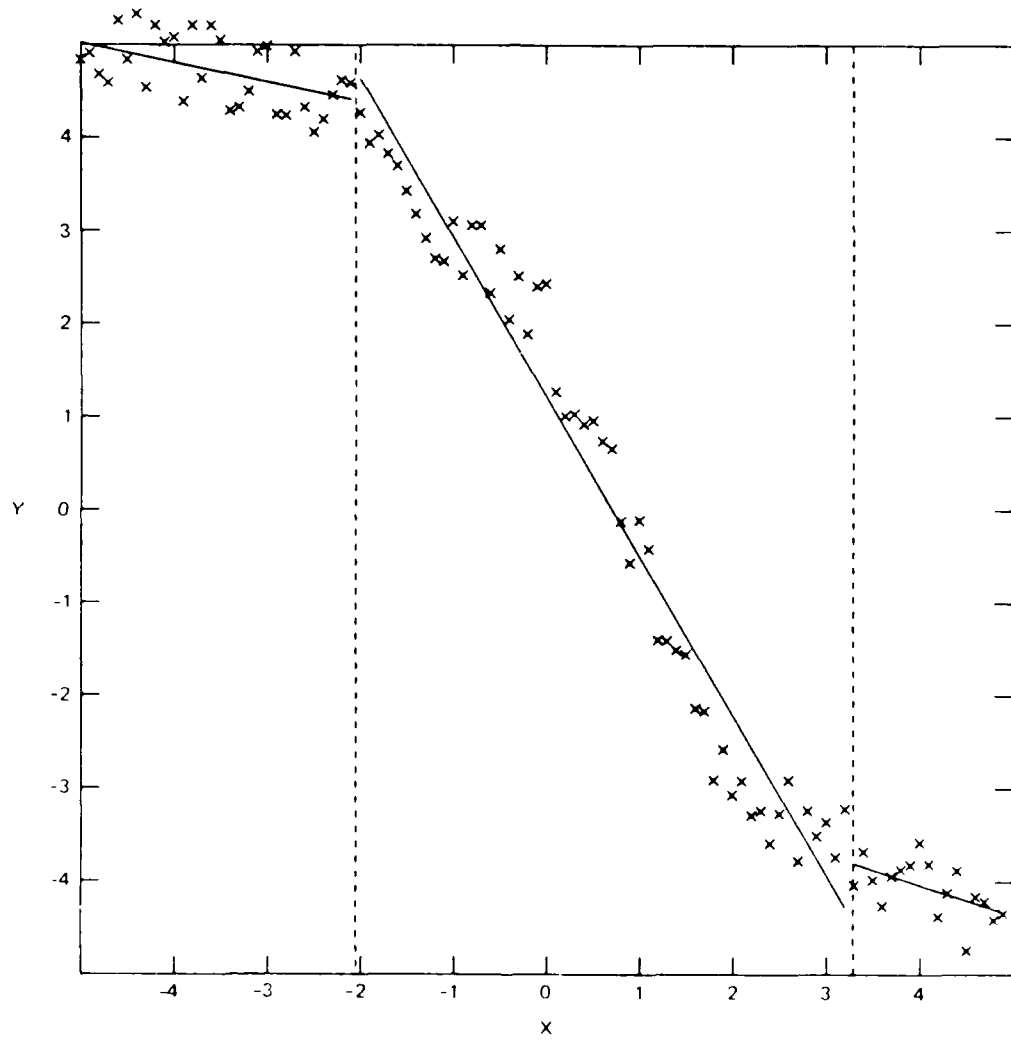


Figure 19. Linear least-squares fits to data over each estimated linear region.

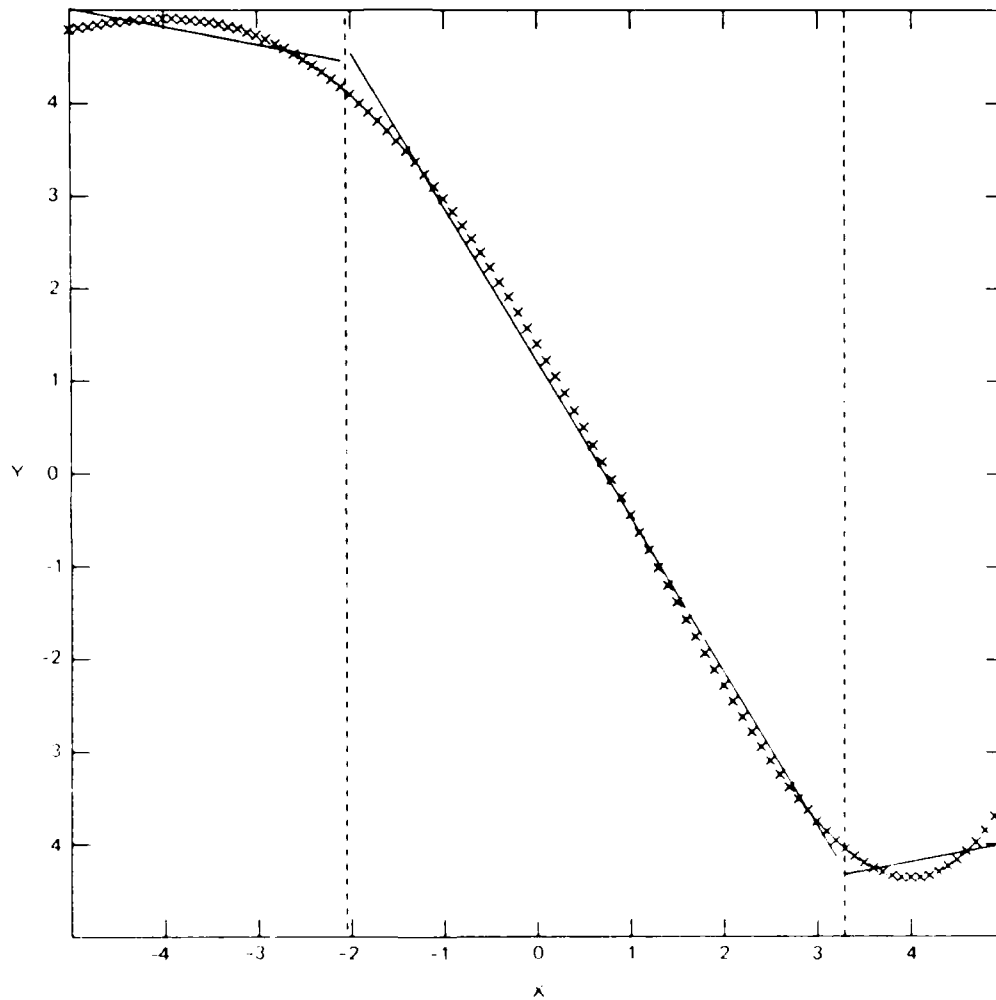


Figure 20. Linear least-squares fits to polynomial over each estimated linear region.

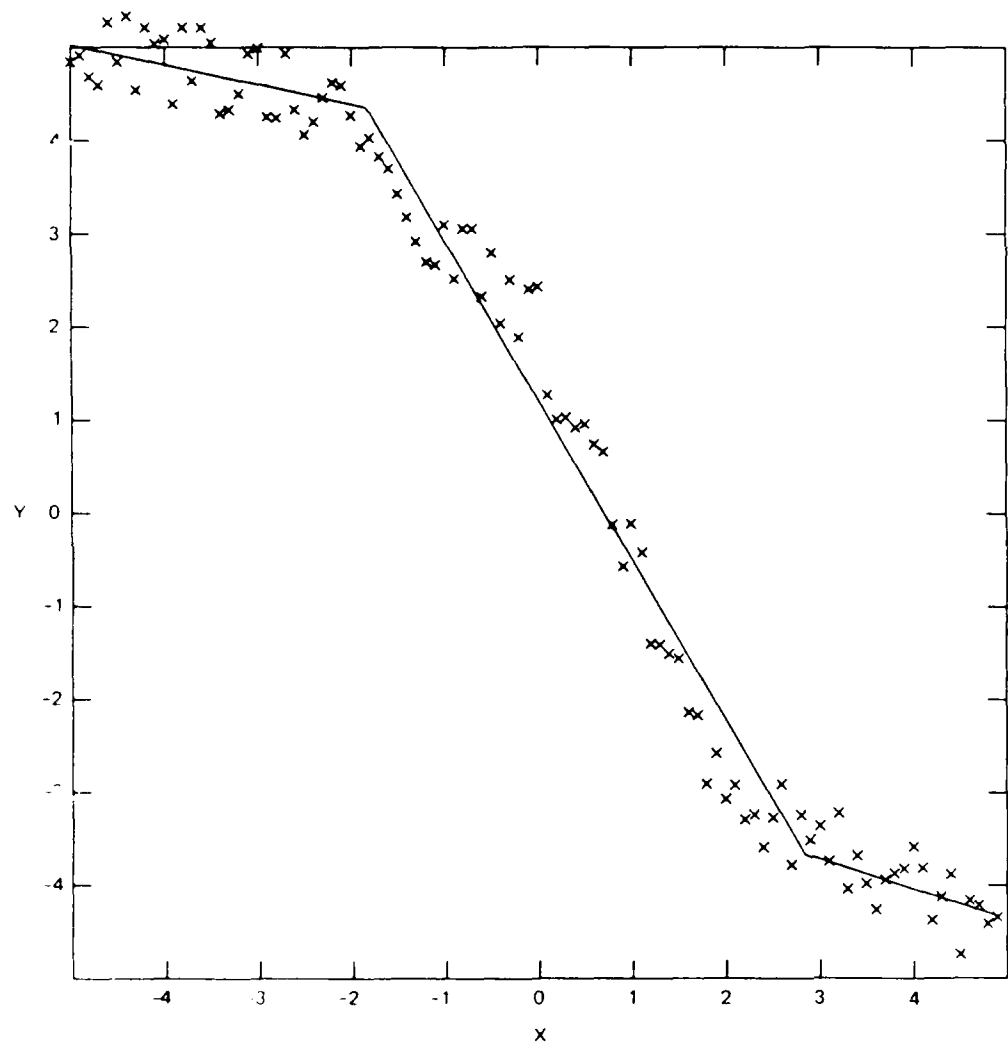


Figure 21. Multisegment fit to data.

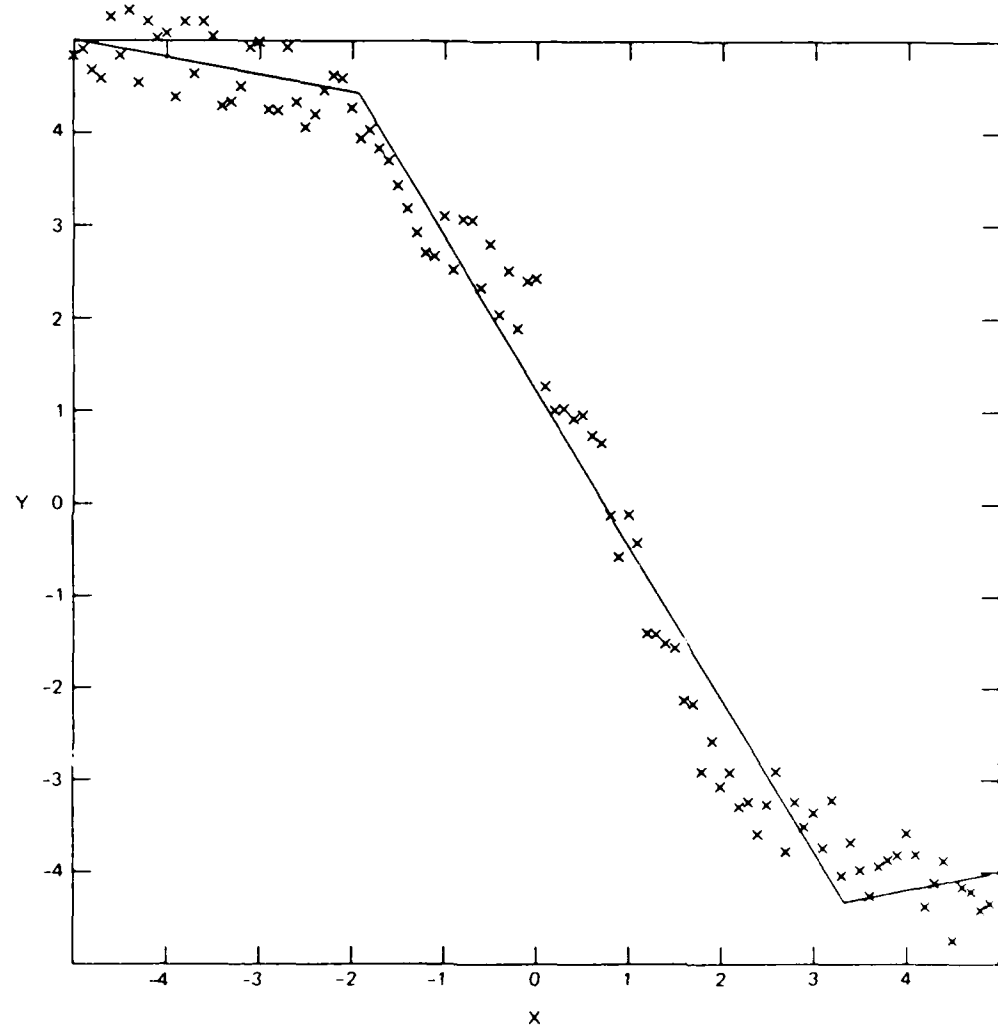


Figure 22. Multisegment fit to polynomial representation of the data.

A.4 CONCLUSION.

We have developed a unique scheme for sorting two-dimensional data into linear regimes. Unlike other methods that fit segments to data, this algorithm determines the number of linear regimes in the data and the ranges of these regions. Because it determines the locations of each region from a polynomial model, the accuracy of the linear fits is dependent upon the polynomial's ability to represent the data. When the polynomial fit accurately represents the data, the linear fits will also accurately represent them. This scheme provides an efficient and objective way to make multisegmented fits to two-dimensional data.

DISTRIBUTION LIST

DEPARTMENT OF DEFENSE

DEFENSE INTELLIGENCE AGENCY
ATTN RTS-2B

DEFENSE NUCLEAR AGENCY

ATTN NANF
ATTN NAWE
ATTN OPNA
3 CYS ATTN RAAE
ATTN RAAE K SCHWARTZ
ATTN RAAE L SCHROCK
ATTN RAAE T WALSH
ATTN RAEE
4 CYS ATTN TTIL

DEFENSE TECHNICAL INFORMATION CENTER
12 CYS ATTN DD

DEPARTMENT OF THE ARMY

HARRY DIAMOND LABORATORIES
2 CYS ATTN SCHLD-NW P
ATTN SLCHD NW R R WILLIAMS (22000)

U S ARMY FOREIGN SCIENCE & TECH CTR
ATTN DRXST SD

U S ARMY MISSILE COMMAND
ATTN DRSMI YSO J GAMBLE

U S ARMY NUCLEAR & CHEMICAL AGENCY
ATTN LIBRARY

DEPARTMENT OF THE NAVY

NAVAL OCEAN SYSTEMS CENTER
ATTN CODE 532
ATTN CODE 54 J FERGUSON

NAVAL RESEARCH LABORATORY
ATTN CODE 4180 J GOODMAN
ATTN CODE 4700 S OSSAKOW
ATTN CODE 4720 J DAVIS
ATTN CODE 4732 B RIPIN
ATTN CODE 4750 P RODRIGUEZ
ATTN CODE 4780 J HUBA

DEPARTMENT OF THE AIR FORCE

AIR FORCE GEOPHYSICS LABORATORY
ATTN LID/J RAMUSSEN
ATTN LIS J BUCHAU
ATTN LS
ATTN LS/R O'NIEL

ATTN LSI/H GARDINER
ATTN LYD/K CHAMPION

AIR FORCE TECHNICAL APPLICATIONS CTR
ATTN TN

AIR FORCE WEAPONS LABORATORY, NTAAB
ATTN NTN
ATTN SUL

DEPARTMENT OF ENERGY

LOS ALAMOS NATIONAL LABORATORY
ATTN D SAPPENFIELD
ATTN D SIMONS
ATTN J WOLCOTT
ATTN MS J ZINN
ATTN R JEFFRIES
ATTN R W WHITAKER
ATTN T KUNKLE

DEPARTMENT OF DEFENSE CONTRACTORS

AUSTIN RESEARCH ASSOCIATES
ATTN J THOMPSON

BERKELEY RSCH ASSOCIATES, INC
ATTN C PRETTIE
ATTN J WORKMAN
ATTN S BRECHT

EOS TECHNOLOGIES, INC
ATTN B GABBARD
ATTN W LELEVIER

JAYCOR
ATTN J SPERLING

KAMAN SCIENCES CORP
ATTN E CONRAD

KAMAN TEMPO
ATTN B GAMBILL
ATTN DASIA
ATTN R Rutherford
ATTN W McNamara

KAMAN TEMPO
ATTN DASIA

MISSION RESEARCH CORP
ATTN B R MILNER
ATTN C LAUER
ATTN C RINO
ATTN D ARCHER

DNA-TR-86-403 (DL CONTINUED)

ATTN: D KNEPP
ATTN: F FAJEN
ATTN: F GUIGLIANO
ATTN: G MCCARTOR
ATTN: K COSNER
ATTN: R BIGONI
ATTN: R BOGUSCH
ATTN: R DANA
ATTN: R HENDRICK
ATTN: R KILB
ATTN: R MORGANSTERN
ATTN: S GUTSCHE
ATTN: TECH LIBRARY

MITRE CORPORATION
ATTN: A KYMMEL
ATTN: C CALLAHAN
ATTN: D RAMPTON, PH D
ATTN: DR D RAMPTON
ATTN: M R DRESP
ATTN: R DRESP

NORTHWEST RESEARCH ASSOC. INC
ATTN: E FREMOUW

PACIFIC SIERRA RESEARCH CORP
ATTN: E FIELD JR
ATTN: F THOMAS
ATTN: H BRODE, CHAIRMAN SAGE

PHYSICAL RESEARCH INC
ATTN: H FITZ
ATTN: J JORDANO

PHYSICAL RESEARCH, INC
ATTN: R DELIBERIS
ATTN: T STEPHENS

PHYSICAL RESEARCH, INC
ATTN: J DEVORE
ATTN: J THOMPSON
ATTN: W SCHLUETER

R & D ASSOCIATES
ATTN: B LAMB
ATTN: C GREIFINGER
ATTN: F GILMORE
ATTN: G HOYT
ATTN: H ORY
ATTN: M GANTSWEIG
ATTN: M GROVER
ATTN: R TURCO
ATTN: W KARZAS

SCIENCE APPLICATIONS INTL CORP
ATTN: C SMITH
ATTN: D HAMLIN
ATTN: E STRAKER
ATTN: L LINSON

SRI INTERNATIONAL
2 CYS ATTN: C RINO
ATTN: D McDANIEL
2 CYS ATTN: T DABBS
ATTN: W CHESNUT
ATTN: W JAYE

TOYON RESEARCH CORP
ATTN: J GARBARINO
ATTN: J ISE

VISIDYNE, INC
ATTN: J CARPENTER